

Automatic Morphological Reconstruction of Neurons from Multiphoton and Confocal Microscopy Images Using 3D Tubular Models

Alberto Santamaría-Pang · Paul Hernandez-Herrera ·
Manos Papadakis · Peter Saggau ·
Ioannis A. Kakadiaris

Published online: 29 January 2015
© Springer Science+Business Media New York 2015

Abstract The challenges faced in analyzing optical imaging data from neurons include a low signal-to-noise ratio of the acquired images and the multiscale nature of the tubular structures that range in size from hundreds of microns to hundreds of nanometers. In this paper, we address these challenges and present a computational framework for an automatic, three-dimensional (3D) morphological reconstruction of live nerve cells. The key aspects of this approach are: (i) detection of neuronal dendrites through learning 3D tubular models, and (ii) skeletonization by a new algorithm using a morphology-guided deformable model for extracting the dendritic centerline. To represent the neuron morphology, we introduce a novel representation, the Minimum Shape-Cost (MSC) Tree that approximates the dendrite centerline with sub-voxel accuracy and demonstrate the uniqueness of such a shape representation as well as its computational efficiency. We present extensive quantitative and qualitative results that demonstrate the accuracy and robustness of our method.

Keywords Neuron segmentation · Neuronal morphology extraction · Machine learning · Multiphoton microscopy images · Confocal microscopy images

A. Santamaría-Pang · P. Hernandez-Herrera · M. Papadakis ·
I. A. Kakadiaris (✉)
Computational Biomedicine Lab, Department of Computer
Science, University of Houston, Houston, TX 77204, USA
e-mail: ikakadia@central.uh.edu

M. Papadakis
Department of Mathematics, University of Houston,
Houston, TX 77204, USA

P. Saggau
Department of Neuroscience, Baylor College of Medicine,
Houston, TX 77030, USA

Introduction

Neurons are regarded as the basic computational subunits in the brain. The morphology of a typical nerve cell (Fig. 1a) consists of a cell body, known as soma, and a number of tubular structures called dendrites. One of the goals of current modern neuroscience is to understand how a single neuron processes information and communicates with other neurons. Achieving this goal requires the study of the bio-physical and bio-chemical interactions that occur within the neuron. By combining optical imaging and computational neuroscience, mathematical models can be created to describe neuronal function. However, the development of such mathematical models requires detailed knowledge of a neuron's morphology.

There are two sets of major challenges to produce a realistic morphological model. The first set of challenges relates to poor image quality. First, the uneven distribution of fluorescent markers inside the cell (Fig. 1b) results in high variations of contrast among the dendritic structures, especially in the smaller branches. Second, a low signal-to-noise ratio is observed in the acquired images due to the different sources of noise (Pawley 2006) that generally do not follow a Gaussian distribution (Fig. 1c). This effect is due to the fact that the excitation power of the laser scanning device is limited to prevent cellular damage. Finally, the Point Spread Function (PSF) imposed by the optics of the microscope creates an anisotropic distortion in the structural image of the cell.

The second set of three major challenges relates to accurate shape modeling. A realistic morphological model should be expressed as a single-branched tree whose starting point is in the center of the soma. Specifically, the challenges in creating a realistic morphological model are: (i)

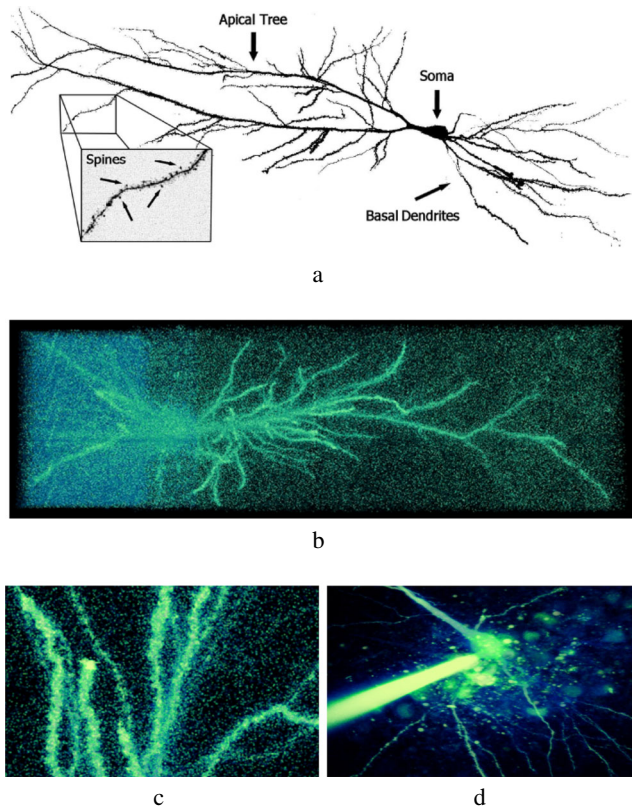


Fig. 1 **a** Illustration of the CA1 hippocampal pyramidal nerve acquired with a confocal microscope, **b** volume rendering of the original data, **c** a detailed image showing the variability in morphology, and **d** an image depicting the artifacts created by external objects (e.g., a micropipette)

identification of the 3D connectivity of the nerve cell in a 3D setting and the accurate estimation of branch lengths, diameters and branch tapering; (ii) developing efficient algorithms since the cell is alive only for a limited amount of time during an experiment; and (iii) excluding any external objects such as the micropipette used to inject the fluorescent marker into the cell (Fig. 1d).

Some of the ideas and methods presented in this paper have been reported in our preliminary reports (Losavio et al. 2008; Kakadiaris et al. 2008) where the feasibility of our method was tested on very limited data consisting of only three neuronal datasets. In this paper, we further refine our methods and mathematically demonstrate why our algorithms are capable of extracting the dendritic centerline with sub-voxel accuracy. In contrast to our earlier approach (Santamaria-Pang et al. 2007a, b), where the outward flux derived from the gray level image was used, the morphological reconstruction methods presented in this paper adopt a probabilistic approach for the segmentation of the neuron from the background. The experimental work is thorough and includes the datasets of ten neurons and four

out of six of the DIADEM datasets (Brown et al. 2011), thus demonstrating the wide applicability of the proposed method.

The contribution of this work is two-fold. First, we introduce a new probabilistic 3D volume segmentation framework for both regular and irregular 3D tubular structures. Rather than proposing a model for segmenting regular tubular structures (Frangi et al. 1998; Sato et al. 1998; Lorenz et al. 1997), our segmentation framework is based on learning features that reflect the local geometry of the tubular object (regular and irregular). Thus, the model can be posed as a linearly separable problem in the domain of the eigenvalues derived from the Hessian matrix.

Second, we present a method for the automatic extraction of the 3D morphology of a neuron modeled as a connected acyclic graph, creating a continuous and unique representation of the 3D neuron morphology. In addition, we present a method to handle topological errors such as detection of crossings. In this setting, the root of the graph corresponds to the center point of the soma (automatically detected), the dendritic paths (optimal paths) correspond to the graph edges, and the dendritic branching points correspond to the graph nodes. This shape representation allows us to reconstruct the 3D neuron morphology in the standard SWC format.

The key advantages of the proposed method are: (i) *explicit multi-scale analysis is not needed*: multi-scale analysis is implicitly performed to detect regular and irregular tubular structures (accomplished by learning centerline points with different variations in diameter, intensity, curvature, and noise); (ii) *learning of structure and noise*: using this machine learning approach, we not only learn the geometrical shapes, but also learn the noise variations intrinsic to the imaging modality; (iii) *general applicability of the method*: the proposed method is straightforward and easily used for the detection of different tubular shapes in the data obtained from various imaging modalities; and (iv) *a unique representation of the 3D morphology with sub-voxel accuracy*: by expressing the dendritic centerline as the optimal path, we can find a unique solution to the problem of minimizing the set of paths that are connected to the root (soma).

The remainder of the paper is organized as follows: in Section “[Previous Work](#)”, previous work in regards to the morphological reconstruction of neurons and the segmentation of irregular tubular structures is presented. In Section “[Materials and Methods](#)”, we present our approach for the segmentation and the morphological reconstruction of nerve cells. In Section “[Results and Discussion](#)”, we report and discuss our results. Concluding remarks are presented in Section “[Conclusions](#)”.

Previous Work

In this section, we review existing methods for neuron morphology reconstruction. We categorize these methods according to their specific characteristics.

The morphological reconstruction algorithms for neurons may be categorized as: (i) *skeleton-based methods* (Dima et al. 2002; Evers et al. 2005; Uehara et al. 2004; Urban et al. 2006; Yuan et al. 2009; Srinivasan et al. 2010; Bas and Erdogmus 2011), where the morphology is reconstructed from the centerline; (ii) *cylinder extraction-based methods* (Wearne et al. 2005; Broser et al. 2004; Zhao et al. 2011; Wang et al. 2011b), where the morphology is reconstructed directly from a given cylindrical model; and (iii) *seed-points graph-based methods* (Santamaria-Pang et al. 2007a; NeuroLucida 2014; González et al. 2009, 2010; Rouchdy and Cohen 2009; Cuntz et al. 2010; Vasilkoski and Stepanyants 2009; Peng et al. 2011; Xie et al. 2010, 2011; Chothani et al. 2011); where seed-point graph-based methods approximate the centerline using a limited number of observations (seeds).

Among the various skeleton-based methods, Dima et al. (2002) used a 3D discrete wavelet transform for the denoising, segmentation, and extraction of the dendritic centerline. Later, Evers et al. (2005) presented a semi-automated method for neuronal morphology reconstruction in which the branching points were manually selected to estimate the centerlines and diameters of cylindrical segments. Wearne et al. (2005) employed a thresholding approach to segment the dendrites. Then, the volume is skeletonized and the diameters are estimated by a Rayburst algorithm. Srinivasan et al. (2010) proposed a method to trace the centerline using moving spheres. Given an initial seed point, the next point is chosen as the voxel that maximizes a Gradient Vector Flow (GVF) score in a neighboring region. Bas and Erdogmus (2011) presented a recursive principal curves tracing algorithm to extract the topology of a neuron. Broser et al. (2004) presented an algorithm based on the nonlinear anisotropic diffusion filtering Perona and Malik (1990) of 3D images. Finally, Zhao et al. (2011) used elliptical Mexican Hat Filters to fit cylinders to the data.

In general, most graph-based methods initially select seed points as candidates and then use seed-point linking algorithms to reconstruct the neuron morphology. Auto-Neuron (AN) is a commercial software included with NeuroLucidaTM (NeuroLucida 2014). This software uses a manual tracing method. First, a number of seed points are generated through manual interaction. Then, the centerline is extracted by connecting the seed points. The major drawback of this method is that the resulting reconstruction may not form a complete tree, thus the user must reconnect the individual subtrees. To reconstruct dendritic

trees, seed points and multiple shortest path search methods are proposed (Rouchdy and Cohen 2009, Xie et al. 2010). Gonzalez et al. (2009) first detected a number of seed points, say N . Then, for a range of K values, they found the minimum weight tree that spanned K of its N vertices and selected the tree that maximized a global objective function. Similarly, Cuntz et al. (2010) reconstructed the dendritic tree from seed points while imposing star-like constraints in the tracing. Vasilkoski and Stepanyants (2009) used a voxel-coding method to recover tree traces. Xie et al. (2011) selected seed points to capture the neuronal structure. Then, a minimum spanning tree approach was used to obtain the optimal tree from those seed points. Peng et al. (2011) created an undirected graph where vertices were image voxels and the edges’ weights were defined by a geodesic metric function. Then, Dijkstra’s algorithm (Dijkstra 1959) was used to obtain the shortest path between a seed point and every other vertex in the graph. Finally, a pruning process was used to remove the redundant structural elements and obtain the final reconstruction. Xiao and Peng (2013) proposed an extension to Peng et al. (2011) by applying a distance transform to the 3D image stack which allows enhancement of the initial tree reconstruction step. Chothani et al. (2011) used a voxel coding algorithm (Vasilkoski and Stepanyants 2009) and active contour approach to obtain the skeleton of the dendritic arbor. Zhao et al. (2009) proposed a tracking algorithm which is initialized with a superellipsoid model into the tube. (Wang et al. 2011a, b) presented a 3D open-curve active contour model where the deforming forces were based on the GVF. Several seed detection methods were presented to automatically initialize the snake model. (Turetken et al. 2012, 2013) proposed to select points in the 3D image stack with high probability to be a tubular structure. Then, a minimal path approach was employed to connect closest points. Finally, the optimal tree was selected using a quadratic mixed integer programming. Breitenreicher et al. (2013) proposed to use a classifier to quantify tubularity of structures. This measure is employed to automatically select

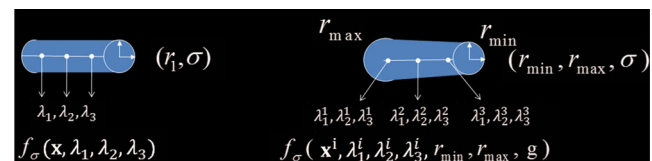


Fig. 2 Depiction of a regular (L) and a generalized (R) tubular model. A regular tubular model is a 3D cylinder with a constant radius and a fixed centerline with constant eigenvalues along the centerline, while a generalized tubular model has a variable radius and the variable eigenvalues in the centerline; the variation depends on: (i) the radius at the given point and (ii) curvature

seed points in the 3D image stack. Then, these seed points are connected to the root of the structure using the shortest path algorithm. Finally, extracted branches with low probability are discarded. The major challenge for both the graph-based and the seed-based methods is the unreliability of the detection of branching points on the reconstructed tree. Tracing methods must detect the linking and branching point from the seeds. In addition, seed points are not guaranteed to be on the centerline, thereby making the estimated centerline different from the true centerline.

Most of the existing algorithms assume an elliptical or semi-elliptical shape of the cross-section of the object of interest (typically vessels). However, when detecting objects with extremely high irregularities in shape (i.e., not semi-elliptical), these algorithms may not perform well, since the assumption of an elliptical shape does not hold true. This is due to: (i) the irregular shape of the dendrites: dendrites do not present a circular or elliptical cross-sectional shape as vessels do; (ii) spines: these are small structures attached to the dendrites that play a crucial role in neuron physiology, therefore it is desirable to enhance and detect them; and (iii) image variability: optical imaging is based on the photonic excitation of a fluorescent dye leading to a different noise model as compared to CT or MRI. Accurate detection of such irregular shapes is necessary for a comprehensive morphological description (Urban et al. 2006; Uehara et al. 2004; Santamaria-Pang et al. 2006, 2007b; Losavio et al. 2008). For a discussion of the advantages and limitations of cylinder-based, skeleton-based and seed point graph-based methods see (Greenspan et al. 2001; Meijering 2010).

Materials and Methods

1 Experimental Data

We applied neuron reconstruction in two types of datasets. The first type of dataset depicts rat hippocampal via CA1 pyramidal neuron cells, acquired with multiphoton and confocal microscopes. The multiphoton data were acquired using a custom-built microscope from neurons loaded with Alexa Fluor 594 dye. Twelve image datasets were collected; each dataset consisted of seven or more partially overlapping stacks with an approximate size of $640 \times 480 \times 150$ each and a voxel size of $0.3 \mu\text{m}$ in the $x - y$ axis and $1.0 \mu\text{m}$ in the z axis. The excitation wavelength was set to 810 nm , while the index of refraction of the lens corresponded to water. Confocal data were acquired with an Olympus Fluoview™ confocal microscope loaded with Alexa Fluor 555 dye. Confocal imaging datasets consisted of three or more partially overlapping stacks with a resolution of $1,024 \times$

$1,024 \times 110$ each; the resolution of each stack was $0.25 \mu\text{m}$ in the x and y axis and $0.5 \mu\text{m}$ in the z axis. The emission and excitation wavelengths were set to 543 nm and 567 nm , respectively, while the numerical aperture and pinhole diameter were set to $0.9 \mu\text{m}$ and $150 \mu\text{m}$, respectively. The index of refraction of the lens corresponded to water. The second type of dataset corresponds to nerve cells from the DIADEM challenge.

2 Online Reconstruction and Functional Imaging Of Neurons (ORION)

Our approach for morphological reconstruction consists of several steps. An outline of the reconstruction is presented in Algorithm 1.

Algorithm 1 ORION

Input: A volume V representing the neuron cell.

Output: An acyclic graph G representing the morphology of the neuron cell.

Step 1: Dendrite segmentation

- 1.1: Estimate the anisotropic tubular features
- 1.2: Estimate the posterior probability $p(\mathbf{x}|\text{centerline})$
- 1.3: Estimate the segmented volume V_S

Step 2: Morphological reconstruction

- 2.1: Detect the soma center point and remove the pipette
- 2.2: Detect the dendritic terminal points (\mathbf{t}_j)
- 2.3: Extract the centerline and reconstruct the tree

Step 3: Post-processing

- 3.1: Detect missed branches
 - 3.3: Connect proximal paths
 - 3.4: Detect crossings
-

Step 1-Dendrite segmentation: We propose a general framework for learning the shape priors for generalized 3D tubular models via implicit scale modeling. Specifically, we estimate a similarity metric function from the eigenvalues of the Hessian matrix that allow us to determine how similar an unlabeled point is to the points in the centerline of the tubular object. In addition, rather than performing computationally expensive multiscale analysis of the eigenvalues, we introduce *implicit scale modeling*, so we learn the distribution of centerline points at different diameters, significantly reducing the computational cost of the algorithm.

Generalized Tubular Models In previous methods, structural features in 2D and 3D have been computed using isotropic data (Frangi et al. 1998; Sato et al. 1998). We consider the general case of objects with an anisotropic aspect ratio. For a fixed σ_{xy} in the x and y axis and for a fixed σ_z in the z axis, with $\sigma_z = \lambda\sigma_{xy}$ where λ is the aspect ratio, we compute the Hessian matrix $H(V)$ of the filtered image by an anisotropic low-pass Gaussian filter G with $\Sigma = \begin{pmatrix} \sigma_{xy}^2 & 0 & 0 \\ 0 & \sigma_{xy}^2 & 0 \\ 0 & 0 & \sigma_z^2 \end{pmatrix}$. The Hessian matrix is computed as,

$$H(V) = \begin{pmatrix} V_{xx} & V_{xy} & V_{xz} \\ V_{yx} & V_{yy} & V_{yz} \\ V_{zx} & V_{zy} & V_{zz} \end{pmatrix}, \tag{1}$$

where $V_{xy} = \frac{\partial^2}{\partial x \partial y} (G * V)$ represents the approximation to the second partial derivative after convolving the image I with an anisotropic Gaussian kernel. Let $\lambda_1, \lambda_2,$ and λ_3 be the eigenvalues of $H(V)$. For isotropic data, we consider the case where $\sigma_{xy} = \sigma_z$. By ordering the eigenvalues of $H(V)$ according to their magnitude ($|\lambda_1| \leq |\lambda_2| \leq |\lambda_3|$), different combinations reveal specific shape information. For example, if $|\lambda_1| \approx |\lambda_2| \approx |\lambda_3| \approx 0$, then there is no structure present; if $|\lambda_1| \approx 0, |\lambda_1| \ll |\lambda_2|$, and $|\lambda_2| \approx |\lambda_3|$, then the structure resembles an ideal tubular structure (Frangi et al. 1998). From those different configurations, analytical functions can be derived (Frangi et al. 1998; Sato et al. 1998; Lorenz et al. 1997). However, a major drawback of these methods is that they are restricted to ideal cylindrical models with a constant diameter. An alternative approach is to learn the 3D priors from the data itself.

Figure 2(L) depicts a regular tubular model. Given a fixed scale σ for the Gaussian filter, the eigenvalues corresponding to the centerline of the regular tubular model are constant. Then, for a fixed radius r_1 and scale σ , the decision function $f_\sigma(x, \lambda_1, \lambda_2, \lambda_3)$ to determine if a point x is in the centerline exclusively depends on the eigenvalues at point x .

The key idea is that a *centerline similarity metric* can be derived from the union of a finite number of center points, having similar geometrical and shape properties. We define a generalized tubular model T based upon local and global shape as: $T = \{r_{\min}, r_{\max}, I, g\}$, where r_{\min}, r_{\max} are the minimum and maximum radii, respectively, I represents the intensity decay from the centerline to the boundary of the tubular model where the intensity decay I of a cross section from a tubular structures is usually modeled as 2D-radial Gaussian which depends on the size of the radius of the tubular structure, and g represents the sequence of the dendrite centerline point locations. Implicit scale is performed by fixing σ and sampling center points along the generalized tubular structure which includes regular tubular models of different radii. Then, the eigenvalues of $H(I)$

along the centerline are different at positions x of the centerline of different radii. Thus, the centerline model can be expressed in terms of local and global shape properties as: $f_\sigma(\mathbf{x}^i, \lambda_1^i, \lambda_2^i, \lambda_3^i, r_{\min}, r_{\max}, g)$.

Figure 3a depicts a generalized tubular model, whose morphological properties include: (i) variation in appearance I from cross-sections (2D-Gaussian profiles), (ii) variable radius from $r_{\min} = 0.5 \mu m$ to $r_{\max} = 1.5 \mu m$ and (iii) the centerline g contains branches, and low and high curvature segments. The voxel size was set to isotropic ($1 \mu m$). Figure 3b depicts the mapping of the eigenvalues as a function of the four individual tubular models. We observe that each cluster corresponds to the

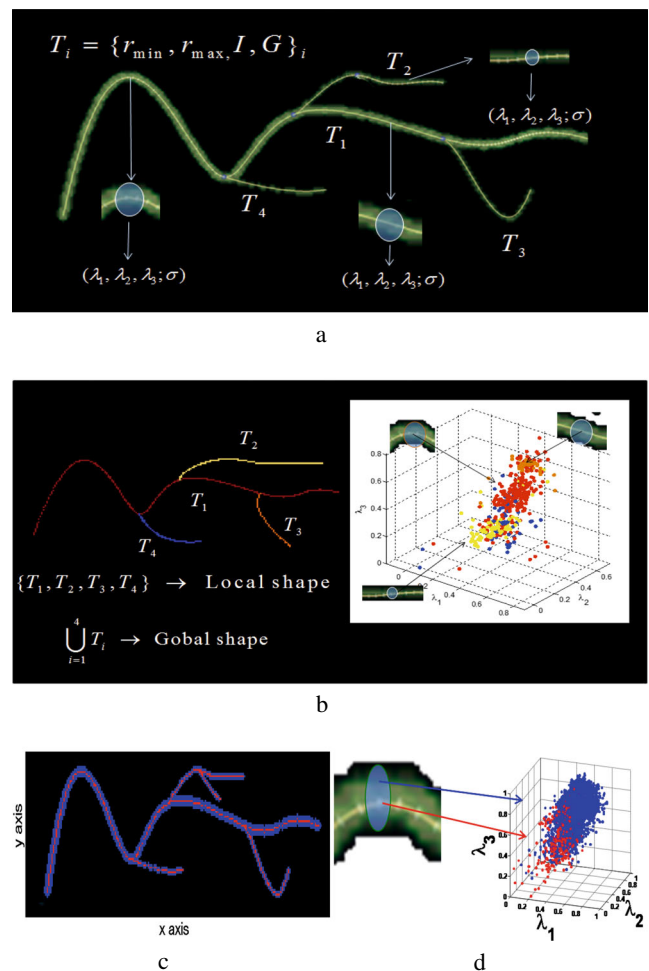


Fig. 3 **a** Depiction of a generalized tubular model. **b** A scatter plot depicting the classes corresponding to the generalized tubular models. **c** Depiction of the data where voxels corresponding to the centerline are marked in red, while voxels corresponding to the non-centerline are marked in blue. For training, positive samples are centerline points (red), while negative samples are the non-centerline and non-background (blue and black). **d** Depiction of the distribution of the normalized eigenvalues

local shape and that the union of all the clusters represents the global shape. Figure 3d depicts the class distribution of the eigenvalues with the centerline labels depicted in Fig. 3c. Note that the probability distribution of the centerline and the non-centerline classes overlap. Thus, we can estimate the probability of an element belonging to the centerline of the tubular object.

Learning Dendrite Centerline Similarity Measures We learn dendrite similarity measures using Support Vector Machines (SVM) (Cortes and Vapnik 1995; Vapnik 1995). SVMs estimate a decision function $f_\sigma(\mathbf{x})$ for any value $\mathbf{x} \in \mathbb{R}^n$. The function $f_\sigma(\mathbf{x})$ is estimated from a set of training vectors $\mathbf{x}_i \in \mathbb{R}^n, i = 1, \dots, l$ with labels $y_i \in \{-1, 1\}$. In our case, the training vectors are the eigenvalues of the Hessian matrix computed at scale σ .

We estimate the similarity measures using the posterior probability $p(y = 1|f_\sigma)$ as:

$$p(y = 1|f_\sigma) = \frac{1}{1 + \exp(Af_\sigma(\mathbf{x}) + B)}, \quad (2)$$

where the parameters A and B are estimated as proposed by Platt (2000).

Figure 4a depicts regions A-E from a volume where region E was used for training and regions A-D for testing. SVM training was performed by grid search with different kernels (linear, polynomial, exponential) and different radii (Eq. (1)) corresponding to: σ_{xy} (0.15, 0.3, 0.45, 0.9) μm , and σ_z (0.5, 1.0, 1.5, 2.0) μm . Positive samples correspond to voxels that belong to the centerline (manually selected) and negative samples are dendritic voxels that do not belong to the centerline. The goal is to construct a dendritic shape model capturing both global and local shape and scale variations. We introduce an implicit scale parameters model by

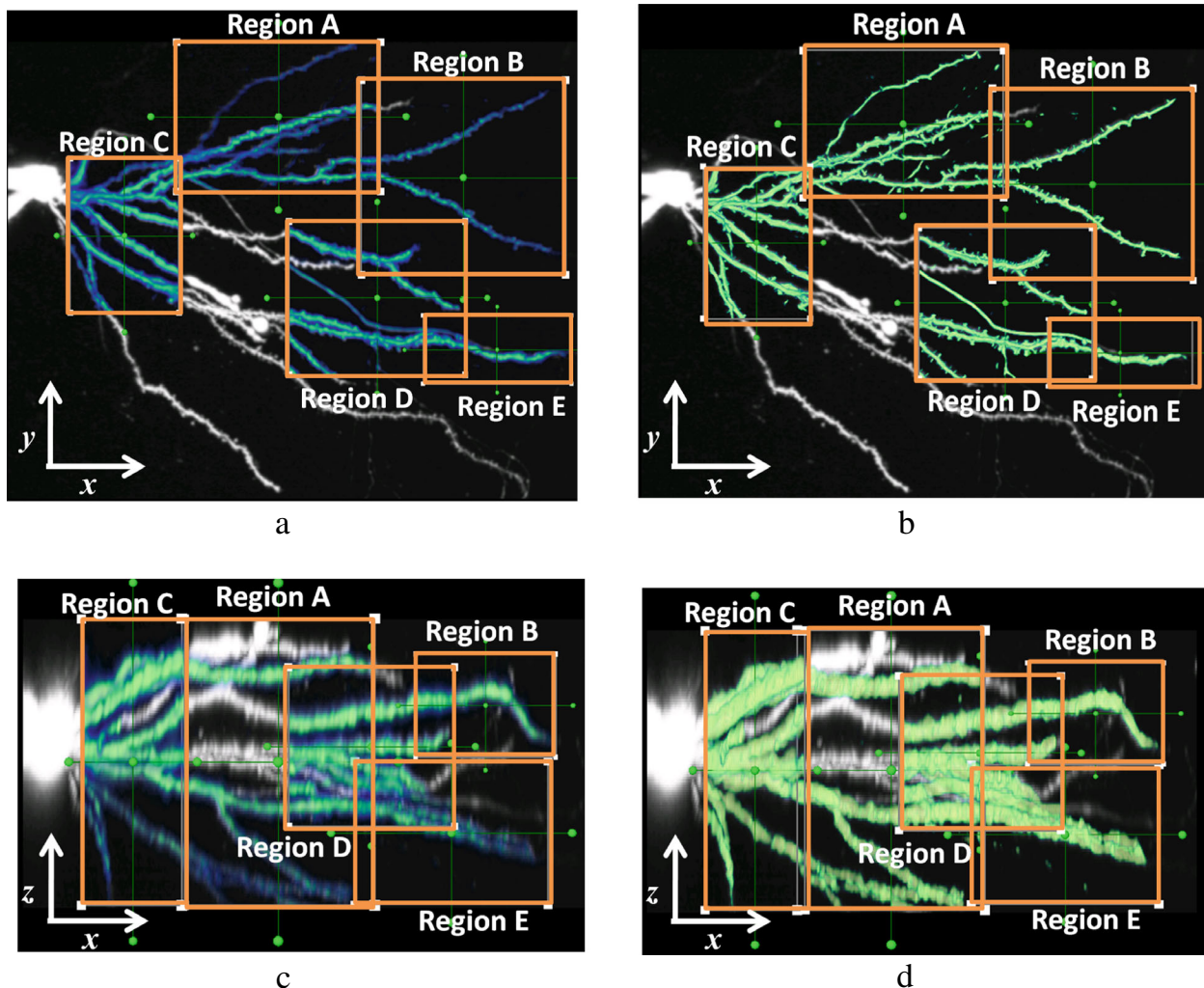


Fig. 4 Illustration of dendritic enhancement: **a, c** a depiction of selected regions in the denoised data where region E was used for training; **b, d** a depiction of the posterior probability $p(y = 1|f_\sigma)$ of the selected regions A-E

selecting dendritic shapes with different diameters. Positive samples are taken from: (i) spines to account for the irregularities from a cylindrical model; (ii) thin and thick dendrites, branching points and low contrast dendrites to account for appearance; (iii) dendrites with high and low variation in curvature; and (iv) different parts of the 3D image stack to account for global and local shape.

SVM parameter estimation was performed with a grid search using three-fold cross-validation. The estimated SVM parameters using a linear kernel for the irregular shape model (Fig. 4a) were: $A = -1.94$, $B = -0.222$, $C = 50$, $b = 8.269$, $\sigma_{xy} = 0.3 \mu m$, and $\sigma_z = 1 \mu m$. Figure 4b, d depict the prediction in the different regions. Figure 5a, c depict the volumetric projection in the $x - y$ and $x - z$ views of two volumes from the DIADEM dataset for which testing was performed. Figure 5b, d depict a volumetric representation of the probability volume obtained by the model trained from a generalized tubular model.

The function for the segmentation is defined as:

$$V_S(x) = o_1(p(x|f)) \vee o_2(V(x)), \tag{3}$$

where \vee is the OR logical operator, the term $o_1(p(x|f))$ is a probabilistic morphological operator, composed of the posterior probability p that a voxel belongs to the centerline (2) and is equal to 1 in regions greater than or equal to a given probability value. This function ensures that the majority of the small dendrites are robustly segmented. The second term $o_2(V(x))$ is a threshold operator that is equal to

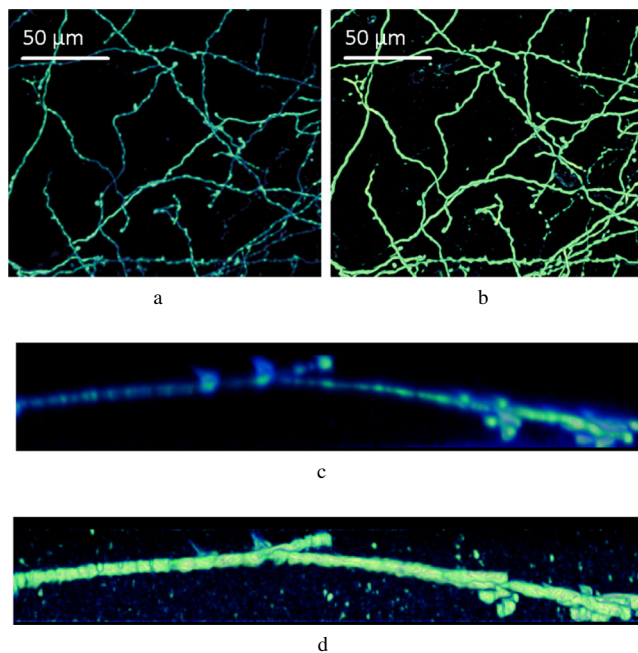


Fig. 5 Illustration of dendritic enhancement, **a, c** volume rendering of the denoised volumes of two different cells in the $x - y$ axis and $x - z$ axis, respectively, **b, d** volume rendering of the probability volume in the $x - y$ axis and $x - z$ axis, respectively

1 in regions greater than or equal to a given intensity value. These operators ensure that wider structures, mainly the soma (not a cylindrical object) and the largest dendrites are segmented. In the rest of this paper, we refer to the volume V_S as the segmented volume that is obtained by applying our segmentation function (3) to the entire cell body (including dendrites). The operators o_1 and o_2 have a significant impact on the segmentation of the dendrites. These values were fixed for most of the stacks to $o_1 = 0.3$ and $o_2 = 0.5 \times \max_x \{V(x)\}$ and were experimentally selected.

Step 2-Morphological reconstruction The morphological reconstruction of a neuron cell expresses the cell anatomy in terms of a single tree representation where each centerline point is connected to its neighbor.¹ To achieve this representation, we introduce a cost function where dendritic centerlines correspond to graph edges and branching and terminal points correspond to graph vertices.

Following Diestel (2005), the centerline of a dendritic arbor can be defined as the set of edges of a finite acyclic graph that satisfies the following properties: (i) each edge is a simple (has no loops) C^2 curve in 3D with a finite length; (ii) only one of the vertices may belong to the soma of the dendrite, if the dendrite contains a soma (this vertex is referred to as the soma vertex); and (iii) each vertex is a branching point, a terminal point, or a soma vertex.

We assume that each dendrite is a connected acyclic graph (all dendrites are trees). Then, the first of the above properties implies that each edge admits a unique parameterization by its arclength. Furthermore, if P is a graph edge, we denote its length by $l(P) = \int_P ds$, where $ds = \sqrt{dx^2 + dy^2 + dz^2}$. If x and y are two vertices, then $d(x, y) = l(P_{x,y})$, where $P_{x,y}$ is the piecewise simple C^2 curve consisting of edges connecting x with y . Since we consider all dendrites to be trees, such a path connecting x with y always exists and is unique (Diestel 2005, Theorem 1.5.1) and $d(x, y)$ is well-defined. Moreover, all vertices of degree 2 or higher are branching points (Diestel 2005, Theorem 1.5.1). The soma vertex is one of the vertices of degree 1, the rest of the vertices consist of the terminal points of the dendritic arbor denoted by t_j . Our approach for morphological reconstruction comprises the following steps:

Step 2.1 - Detection of the Soma Center-Point (s_0) and Pipette Removal This point is designated as the soma vertex of the dendrite. The soma-pipette volume is represented as: $V_{SP} = V_S \cup V_P$, where V_S and V_P are the soma and pipette volumes, respectively. The objective is to automatically: (i) find s_0 , and (ii) remove V_P , if present.

¹Loops are not allowed in a tree structure.

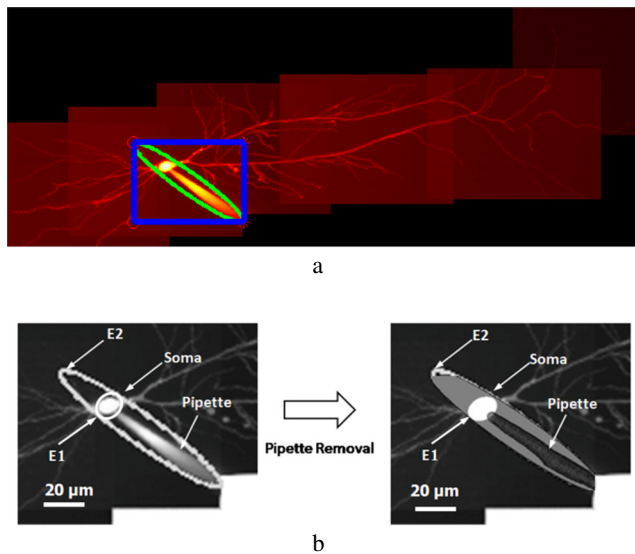


Fig. 6 **a** A depiction of the additive projection along the z axis of a neuron cell; lines in *blue* define a region of interest obtained from the ellipse marked with *green* which encloses the soma and pipette. **b** A depiction of pipette removal: (*left*) ellipse E_2 enclosing the pipette from the projection along the z axis, and (*right*) ellipse E_2 enclosing the soma and pipette

Given that the pipette carries the fluorescent dye, it will produce the highest illumination making the soma and the pipette are the brightest and longest objects along the z axis (Fig. 6a). The estimation of the soma center point s_0 is presented in the following steps. First, we segment the soma-pipette V_{SP} as follows, an ellipse is fitted² to the soma-pipette region obtained from the additive projection along the z axis. We refer to such an ellipse as E_2 (Fig. 6b). Similarly, an ellipse inside E_2 , enclosing only the soma, is detected. We refer to this ellipse as E_1 . Let V_{SP} be the 3D volume for which $Q_{x,y}(V_S) = E_2$, where $Q_{x,y}$ is the projection with respect the $x - y$ plane. Let DT denote the distance transform (Rosenfeld and Pfaltz 1968). The soma center point $s_0 = (x_{s_0}, y_{s_0}, z_{s_0}) \in V_{SP}$, is the point with the largest distance from the border with respect to the volume, $DT(V_{SP})$, such that its corresponding x, y coordinates are in the soma, that is: $(x_{s_0}, y_{s_0}) \in E_1$. The pipette is removed by fitting a 3D cylinder that encloses the pipette volume, and then removing those voxels which are inside the 3D cylinder but not in the soma. To construct such a 3D cylinder, the pipette medial axis is computed as the minimal path from s_0 (soma center) to the farthest point in the pipette Q_0 in the distance map volume $DT(V_{SP})$.

Step 2.2 - Detection of Dendritic Terminal Points t_j To determine terminal points, the algorithm detects voxels in

²The coordinates of the points in the soma-pipette region are used to obtain the center of the ellipse given by the mean of the points and the semi-axis of the ellipse given by the covariance matrix.

the tip of the dendrite. To this end, let V_D be the discrete dendritic volume (i.e., the set of foreground voxels contained in the segmentation of Step 1) and dt be a distance function. Set $k = 0$ and $dt(s_0) = 0$. At step $k = 1$, dt is set to be equal to one at all order-one neighbors of s_0 contained in V_D , where order-one neighbors are defined as 27 neighborhood. A voxel at which dt is defined is referred to as visited. At step $k = 2$, dt is set to be equal to two at all order-one neighbors of all the voxels for which dt is equal to one and are contained in V_D and have not been visited at step $k = 1$. The reader can realize that the step $k = 2$ is actually the inductive step and that each voxel can only be visited once, so dt has a unique value at each voxel. At this step dt is set to be equal to two at each order-one neighbor inside V_D of a voxel for which dt was set equal to one. Therefore, if (x_1, y_1, z_1) and (x_2, y_2, z_2) are voxels connected inside V_D (i.e., $\max\{|x_i - y_i| \leq 1 : i = 1, 2, 3\}$), then $|dt(x_1, y_1, z_1) - dt(x_2, y_2, z_2)| \leq 1$. Now, consider a partial ordering between voxels inside V_D . We define a chain connecting u and v if there exists a set of voxels $u = u_0, u_1, \dots, u_k = v$ such that u_{i-1} and u_i are connected for all i and $dt(u_{i-1}) < dt(u_i)$. Chains are partially ordered by inclusion. Maximal chains start at s_0 and terminate at a voxel which can be considered as a terminal dendritic point. This is true because $dt(s_0) = 0$ and if t is the voxel in a maximal chain with the maximum value of dt on this chain, then t is not connected to any other voxel in V_D with a value of dt exceeding $dt(t)$. Thus, all of the order one neighbors of t neither belong to V_D nor dt has a value equal to $dt(t) - 1$. Hence, t belongs to the boundary of a dendritic branch which is (theoretically) perpendicular to that branch's centerline. This point is identified with the dendritic terminal point of this branch. Figure 7 depicts the voxels that have been identified as dendritic terminal points (marked as green). At step $k = 1$, the order-one neighbors of the soma vertex (red point) are indicated as the white regions (W_1) around the red point. At step $k = 2$, the order one-neighbors of W_1 are indicated as gray regions (G_1) around W_1 . At step $k = 3$, the order one-neighbors of G_1 are indicated as white regions (W_2) around G_1 and so on.



Fig. 7 A visualization of the dendritic terminal points as *green points* and the soma vertex s_0 as a *red point*

Step 2.3 - Centerline Extraction and Tree Reconstruction

An efficient algorithm to construct a graph tree $T = (V, E)$ with sub-voxel accuracy is presented in this Section. Its edges coincide with the dendritic centerline and its vertices are either the terminal points or the soma point. To construct this tree, our ORION method finds the edge P_j from each terminal point t_j to the soma center point s_0 as the optimal path with respect to a cost volume $F > 0$.

A cost function $F(\mathbf{x}) = g(DT(V_D(\mathbf{x})))$ is defined, where V_D is the segmented volume, $DT(V_D(\mathbf{x}))$ is the minimum distance from \mathbf{x} to the boundary of the segmented volume and $g(\mathbf{x}) = e^{-\alpha \cdot \mathbf{x}}$. The constant α in the cost function F is chosen so that it penalizes proximal points to t_j and points close to the dendritic surface while it is negligible between the soma center point s_0 and any non-proximal to s_0 point $\mathbf{x}_0 \in V_D$. Specifically, the value $\alpha = 15 \times \max_x \{DT(V_D(\mathbf{x}))\}$ so that the minimum value of the function $F(\mathbf{x})$ is equal to \exp^{-15} (very close to zero) and the maximum is equal to one (at the dendritic surface). Following Hassouna et al. (2005), the optimal path P_j from t_j to s_0 can be found by solving the minimization problem:

$$T(P_j) = \min_c \int_{t_j}^{s_0} F(c(s)) ds, \tag{4}$$

where $c(t) = \{x(t), y(t), z(t)\}$ and $ds^2 = dx^2 + dy^2 + dz^2$ is the Euclidean arclength. An explicit solution to compute any given P_j , given a terminal point t_j along the centerline of the tubular object, is given by the Eikonal Equation (Sethian 1996):

$$\|\nabla T(\mathbf{x})\| = F(\mathbf{x}), \tag{5}$$

where $T(s_0) = 0$. Each P_j is detected by following the gradient of $T(\mathbf{x})$ from the terminal point t_j to s_0 . In the case of a single dendrite, the P_j is extracted by marching along the gradient of the 3D-front, induced by F , propagating from the terminal point to the soma center point³ s_0 . Since the extracted P_j correspond to points in the stack, the radius at each point $\mathbf{x} \in P_j$ is given by the computed distance transform $DT(V_D(\mathbf{x}))$ from the segmented volume. Note that the SVM probabilities were not used to define the cost function $F(\mathbf{x})$. We prefer to use $DT(V_D(\mathbf{x}))$ because the distance transform of the segmentation will provide high values close to the centerline and therefore the front propagation will propagate faster close to the centerline. The SVM probabilities are very close to one inside the neuron, thus the front propagation will not propagate faster across the centerline.

Figure 8 depicts a 2D projection of the front propagation in a typical volume. Note that in Fig. 8a the front rapidly

³The solution of Eq. (4) coincides with the centerline of each dendritic branch since small distances of a voxel from V_D are penalized and the only points that are equidistant from the dendritic boundary are those of the centerline.

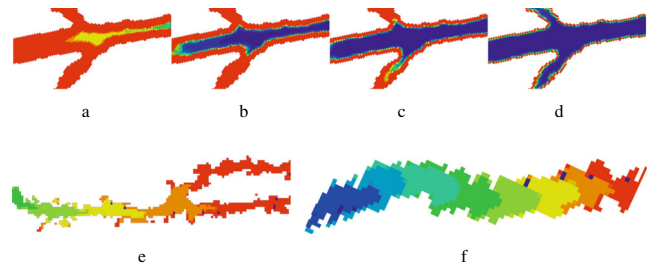


Fig. 8 A visualization of the 3D front propagation along the centerline of the tubular object. **a–d** 3D front propagation in a tubular region (the topology of branching dendrites is naturally modeled, always moving along the centerline); **e, f** 3D front propagation in dendritic structures with small diameters. In this color map, blue denotes the minimum value while red denotes the maximum value

expands in the center, and gradually travels along the centerline of the bifurcations (Fig. 8b–d). Figure 8e depicts the front propagation in a 2D section of a thin dendrite with two branches and Fig. 8f depicts the front propagation in a single dendrite.

In the case of a single dendrite, the P_j is extracted by marching along the gradient of the 3D front from the terminal point to the soma center point s_0 . We now present a theoretical result to construct a Minimum Shape-Cost (MSC) Tree in linear time with respect to the terminal points within sub-voxel accuracy:

Theorem 1 MSC Tree Let $F > 0$ be the cost function defined in Eq. 5, let $\{t_j : j = 1, 2, \dots, N\}$ be a set of N terminal points such that $T(t_1) > T(t_2) > \dots > T(t_N)$, and $s_0 \in F$ be a starting point. Then, a unique (minimum cost) tree (V, E) can always be constructed, where the vertices V consist of the soma, the terminal points t_j and the branching points, and E are the edges that form the dendritic centerline.

Proof Assume that the starting point s_0 (soma center point) is known, $F > 0$, and there are N terminal points. For every terminal point t_j , exists a unique path connecting t_j to s_0 . For $N=1$, the result is evident. For $N=2$, there are two possibilities: $P_1 \cap P_2 \neq \emptyset$ or $P_1 \cap P_2 = \emptyset$. If $P_1 \cap P_2 = \emptyset$, then P_1, P_2 is the tree representation. If

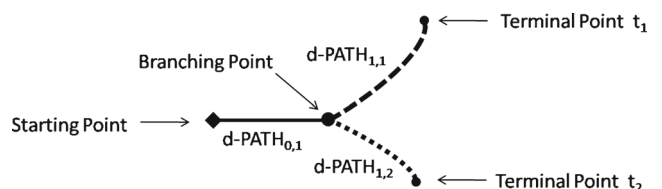


Fig. 9 A schematic depicting the general principle of constructing a graph when tracing the optimal path from the terminal points to the starting point

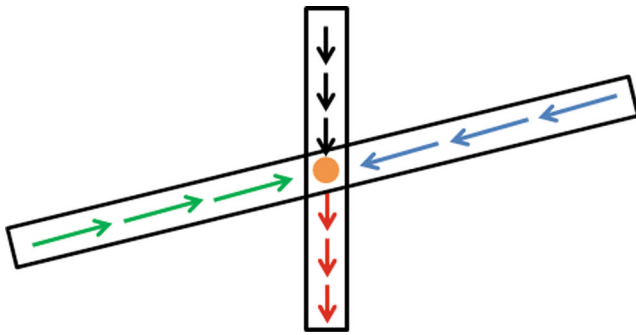
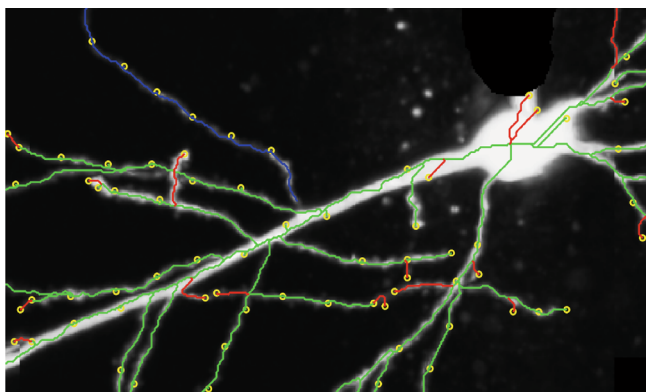
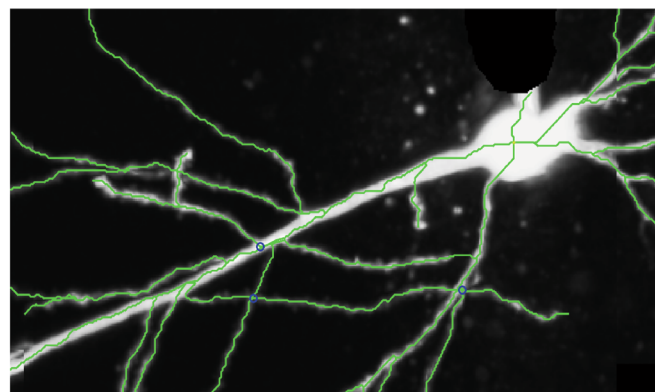


Fig. 10 Crossing can be detected in the graph representation of the reconstruction as three-furcation nodes. Green, black and blue arrows depict the paths of the three parents of the node depicted as orange circle while red arrows depict the path of the node. Two paths (black and red) follow the same direction and the remaining two paths (green and blue) have opposite direction

$\mathbf{P}_1 \cap \mathbf{P}_2 \neq \emptyset$, then exists a point $b_{12} \in \mathbf{P}_1 \cap \mathbf{P}_2$ such that $T(b_{12}) > T(x)$ for all $x \in \mathbf{P}_1 \cap \mathbf{P}_2$. Since the solution to the minimization problem (4) coincides with the centerline of the tubular structure, the section of the paths \mathbf{P}_1 and \mathbf{P}_2 from b_{12} to s_0 is identical. Note that, $\mathbf{P}_1 \cap \mathbf{P}_2$ coincides with the centerline from b_{12} to s_0 and b_{12} is a branching point of the dendritic arbor. This procedure obtains the tree with terminal points $\{t_1, t_2\}$ and the branching point b_{12} whose edges are the sub-paths $\{\mathbf{P}_{01}, \mathbf{P}_{11}, \mathbf{P}_{12}\}$ such that $\mathbf{P}_1 = \mathbf{P}_{01} \cup \mathbf{P}_{11}$ and $\mathbf{P}_2 = \mathbf{P}_{01} \cup \mathbf{P}_{12}$. Assume that given N terminal points, we construct a tree with N terminal points and that we are given an $N+1$ terminal point. Following this inductive argument, we can then construct a tree with $N+1$ terminal points. Tree uniqueness follows from the path optimality. Figure 9 depicts the MSC tree given two terminal points t_j . The dashed lines correspond to paths that are visited only once, while solid lines are paths visited twice. \square



a



b

Fig. 11 a A depiction of the detected centerline by the different steps. Green paths are detected using Step 2 while blue and red paths are detected using the first and second approach

Step 3-Post-processing The previous approach for morphology extraction assumes that the segmentation consists of a single connected component. However, there are usually more than one connected components in the segmentation due to gaps in the image stack or dendrites with low intensity. In addition, it may miss some branches due to “loops” resulting from choosing a coarse PSF. Insufficient spatial resolution may show that the volume has a loop when parts of the tubular structure are very close to each other. Furthermore, the previous approach is not able to identify branches crossing as they are identified as branches trifurcating. Thus, a post-processing step is proposed to handle these errors.

Step 3.1 - Detect missed branches The first approach to detect branches missed by Step 2 of our algorithm consists of detecting the optimal paths for each connected component in the segmentation $V_S(x)$. First, every connected component $C_i(x)$ from the segmentation $V_S(x)$ is identified using 6 neighbors connectivity. Then, our morphology extraction algorithm (Step 2) is repeated for each connected component $C_i(x)$, where $V_S(x) = C_i(x)$ and the soma vertex $s_{0,i}$ is initialized as

$$s_{0,i} = \arg \max_x \{DT(C_i(x))\}$$

the point $x \in C_i(x)$ with the largest distance from the border with respect to the volume $C_i(x)$.

The second approach consists of detecting branches missed due to loops in the segmentation. Given a connected component $C_i(x)$ and the detected dendritic paths P_i (optimal paths) of the connected component $C_i(x)$, first, candidate points \mathcal{C}_i to belong to the dendritic paths in $C_i(x)$ are detected. These candidate points are detected as local maximum of the distance transform $DT(C_i(x))$. Note that these points must be close to the detected optimal paths P_i

from Step 3.1, respectively. **b** The morphological reconstruction of the dendrite. Blue circles depict the nodes that were detected as crossings

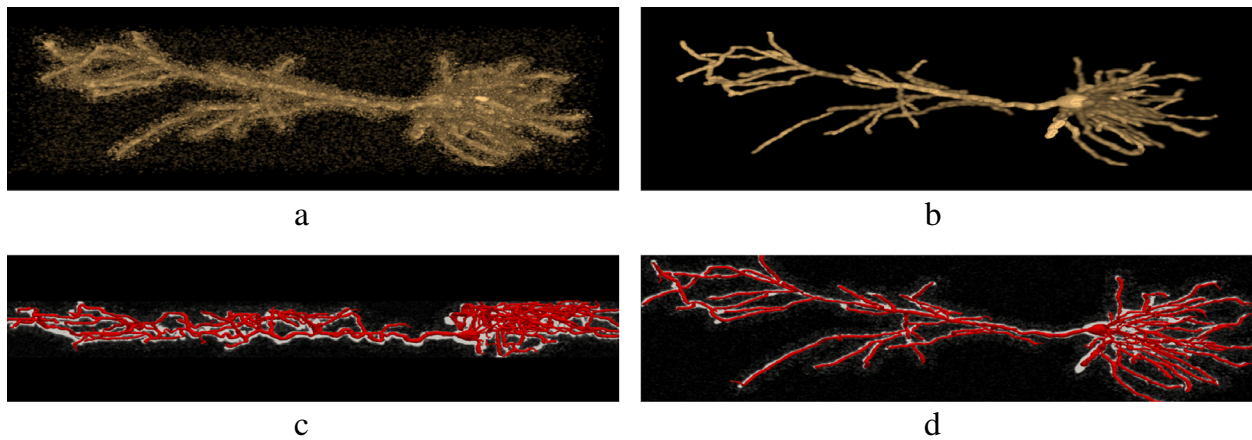


Fig. 12 A depiction of validation in Phantom A: **a** a volumetric representation of a computational phantom; **b** a depiction of the phantom with added noise; **c, d** overlay of the morphological reconstruction with the MIP of the noisy volume

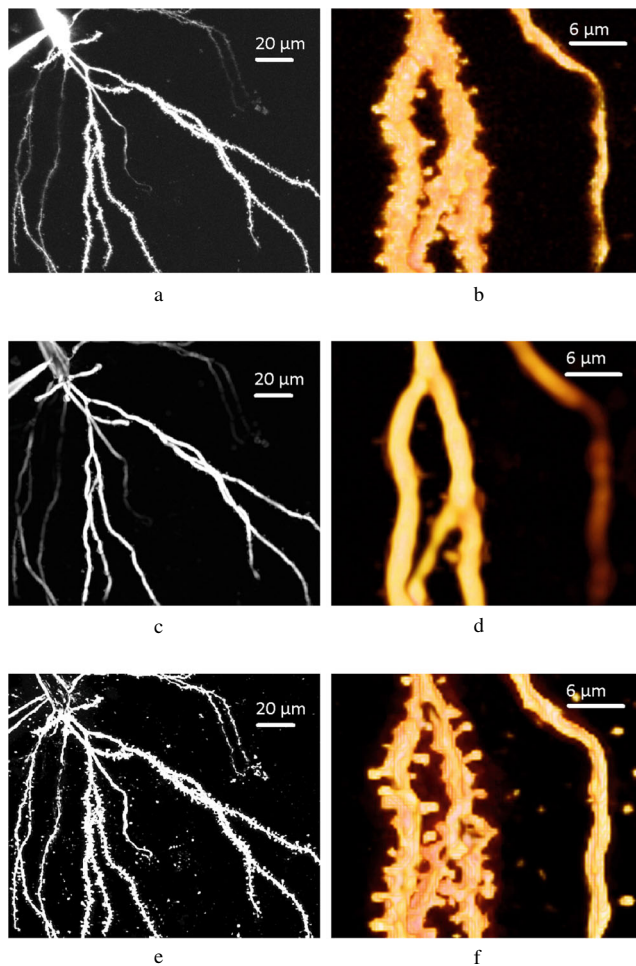


Fig. 13 **a** a depiction using maximum intensity projection in the x, y axis of a typical multiphoton stack; **c, e** the probability maps obtained from the methods of Sato and ORION applied to Fig. 13a, respectively; **(b, d, f)** visualization of details from the volumes depicted in **(a, c, e)**

since the cost function $DT(V_{SP})$ used to detect the optimal paths has low values close to the center of the segmentation and high values close to the boundary. Thus, the detected optimal paths P_i are near to the center of the segmented volume. In order to detect missing branches due to loops, the closest Euclidian distance between each candidate point \mathcal{C}_i and the points in the detected optimal paths P_i is computed. If the Euclidian distance of a candidate point \mathcal{C}_i is smaller than a predefined threshold (four times the mean radii of the points in the detected optimal paths) the candidate point is removed which means that there is a detected optimal path P_i near to the candidate point. Note that some candidate points \mathcal{C}_i may have not been removed because there can be undetected optimal paths due to loops in the segmentation. Then, given a point $p_k \in \mathcal{C}_i$ the optimal paths P_k from p_k to the soma vertex $s_{0,i}$ is computed using Eq. 4. Let P_M be the optimal path P_k with the largest geodesic distance. Thus, P_M is added to the detected optimal paths P_i and the point p_M is removed from \mathcal{C}_i . The process is repeated until all the candidate points are removed. Figure 11a depicts the detected optimal paths from Step 2 in green lines while the detected optimal paths from the first and second approach from Step 3.1 are depicted in blue and red lines, respectively. Finally, the terminal points of the optimal paths are plotted as yellow circles. Note that Step 3.1 allows detection of many branches that were missing in Step 2.

The proposed approach to extract the optimal paths may have detected spurious branches due to spines. Those branches are disregarded by identifying segments with length smaller than a given threshold.

Step 3.2 - Connect proximal paths In the case that more than one connected component was detected in the segmentation, a merging process is proposed to connect the

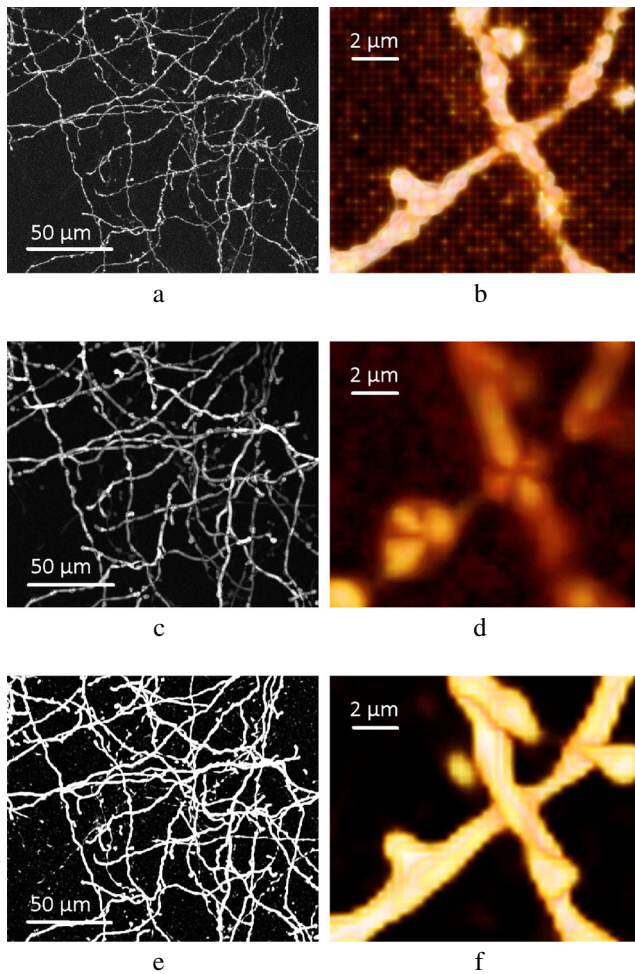


Fig. 14 **a** A depiction using maximum intensity projection in the x, y axis of Neocortical Layer 1 Axon stack from DIADEM dataset; **(c, e)** the probability maps obtained from the methods of Sato and ORION applied to **(a)**, respectively; **(b, d, f)** visualization of details from the volumes depicted in **(a, c, e)**

dendritic paths from different connected components $C_i(x)$. At this stage, optimal paths P_i were detected for each connected component $C_i(x)$, the terminal points \mathcal{T}_i of these paths are detected since terminal points are used to merge the detected optimal paths. First, the optimal path P_i used for merging must be selected. The optimal path P_m used for merging is selected as the detected optimal path P_i with minimum distance between the terminal points \mathcal{T}_i and the points from the detected optimal paths from the other connected components. Note that only one terminal point $\mathcal{T}_{m,o}$ from the optimal path P_m must be used for merging since a single segment is used to connect two different paths, otherwise loops in the morphological reconstruction can be introduced. Thus, given a terminal point $\mathcal{T}_{m,s}$ from the selected optimal paths P_m , this point is connected to a single point belonging to any of the other optimal paths. The

optimal path $P_{m,s}$ for connecting $\mathcal{T}_{m,s}$ to the other paths is detected as

$$T(P_{m,s}) = \min_{c, p \in P_i | i \neq m} \int_p^{\mathcal{T}_{m,s}} F(c(s)) ds,$$

where the cost function F is defined as V^{-1} and V is the 3D image stack. Finally, a connecting cost is assigned to each candidate merging path $P_{m,s}$. Note that human operators usually connect branches based on intensity, distance and branch orientation. These features are employed to compute three cost functions which are combine to compute the total cost of merging a fixed path. The first cost function c_1 is associated with the intensity and penalizes paths with low intensity and it is computed as the average intensity of the 3D image stack along the path $P_{m,s}$. The second cost function c_2 is associated with the length of the path, it penalizes large connections and it is defined as $c_2 = \exp\left(\frac{-L(P_{m,s})}{a}\right)$, where $L(P_{m,s})$ is the length of the path $P_{m,s}$ and a is a constant that controls the sensitivity of the penalization. Finally, the third cost function c_3 is associated with the branch orientation, it penalizes paths having sharp changes in direction. Few points (usually 25) in the vicinity of the terminal point $\mathcal{T}_{m,s}$ and belonging to the path P_m are selected. The branch orientation σ_1 is computed using Principal Component Analysis (PCA) as the first principal component of the points. On the other hand, few points are also selected in the vicinity of $\mathcal{T}_{m,s}$ but belonging to the path $P_{m,s}$ and the branch orientation σ_2 is computed as described above. Then, $c_3 = \langle \sigma_1 \cdot \sigma_2 \rangle$, is the dot product between σ_1 and σ_2 . Note that if σ_1 and σ_2 have approximately the same direction then c_3 is close to one while branches with opposite direction have c_3 close to negative one. Finally, the total cost of merging from terminal point $\mathcal{T}_{m,s}$ is defined as

$$T(\mathcal{T}_{m,s}) = c_1 \times c_2 \times c_3,$$

this cost is computed for each terminal point $\mathcal{T}_{m,s}$ and the path $P_{m,o}$ associated with the terminal point $\mathcal{T}_{m,o}$ with maximum cost is selected as the merging path. Then, Step 3.2 is repeated until there are no paths to merge.

Step 3.3 - Detect crossings One topological error is branch crossing and this is easily corrected by our algorithm due to the connected acyclic graph representation. The first property of branch crossing in the graph representation is that they appear as nodes with three or more parents. The second property due to extracting the paths by propagating from terminal points to the soma center is that the path of one parent have similar direction as the path of the node with three or more parents and the paths of the two remaining parents have opposite directions (see Fig. 10). These properties are taken into consideration to identify if a node with three or more parents is a real tri-furcation point or is a crossing. First, nodes with three or more parents are identified and

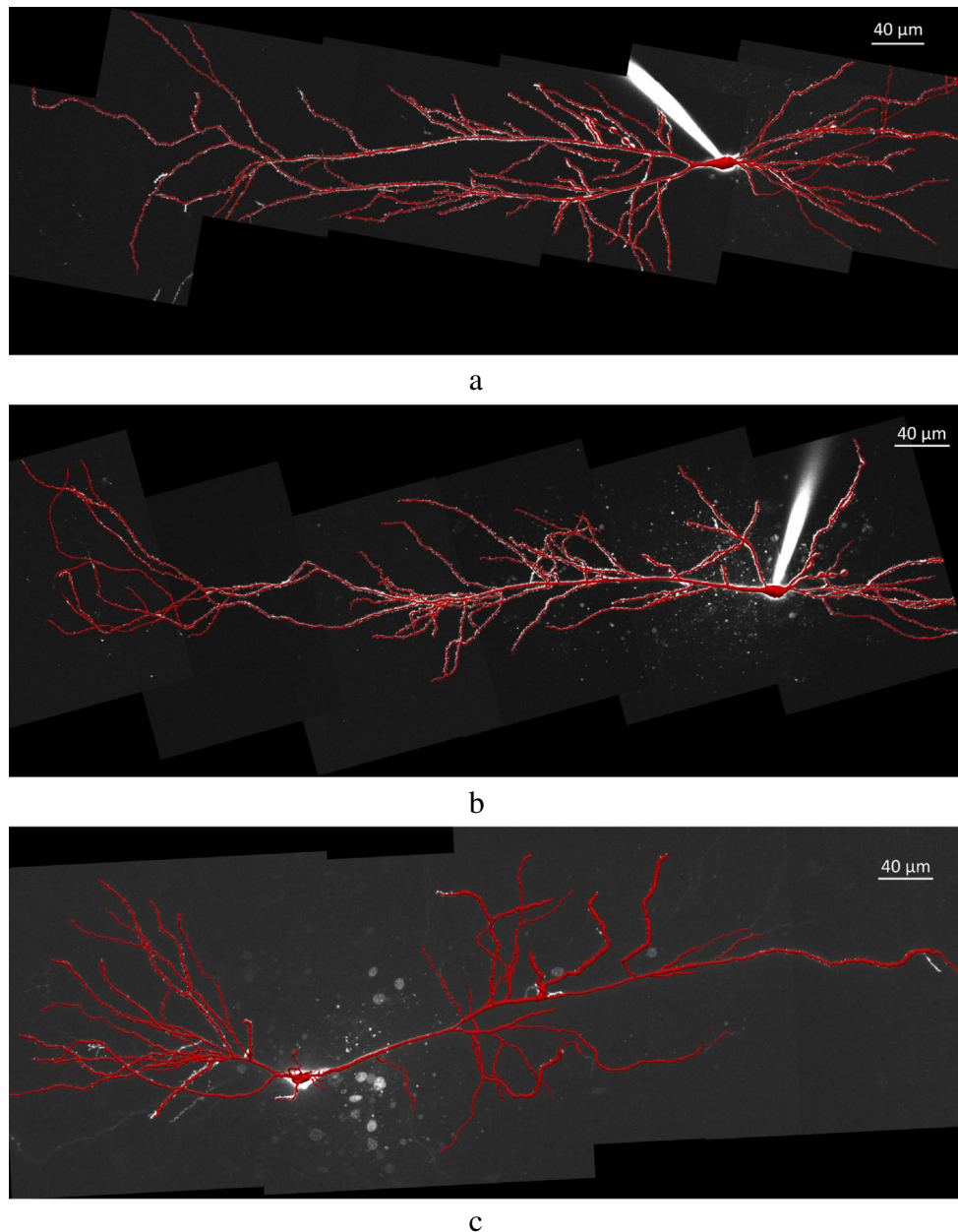


Fig. 15 A comparison of the reconstruction quality in different cells: (a, b, c) the morphological reconstruction of CA1 pyramidal neurons corresponding to cells A, B, and C, respectively

the orientations (o_1, o_2, \dots, o_n) of the node and the parents are computed as described in the previous step for the computation of the branch orientation cost. From the second property, if there is a crossing then the dot product of two directions should be close to one and the dot product of the remaining two should be close to negative one. Thus, all the possible combinations of the directions (o_1, o_2, \dots, o_n) are computed using only four elements $(o_{s1}, o_{s2}, o_{s3}, o_{s4})$. For each combination, the function to detect crossing is defined as:

$$f_c = | \langle o_{s1} \cdot o_{s2} \rangle - \langle o_{s3} \cdot o_{s4} \rangle |,$$

if there is at least one combination with $f_c > 0.90$, then the node is detected as a crossing. Otherwise, it is detected as a branch trifurcating. Figure 11b depicts the detected crossing as a blue circle.

Results and Discussion

In this section, results on: (i) computational phantoms; (ii) datasets from confocal and multiphoton imaging; and DIA-DEM dataset are presented. Results were obtained using a

workstation with a 64-bit processor, eight cores and 12 GB of RAM. The software was implemented in Matlab and ITK.

Synthetic Data The computational phantom that was used for validation is depicted in Fig. 12 and corresponds to the neuron labeled as *n120* from the Duke-Southampton database (Duke/Southampton 2013) with dimensions of $748 \times 316 \times 114$ units. Noise derived from a Poisson model is added in several layers as described by Santamaría-Pang et al. (2008). Figure 12b depicts the volumetric rendering of the denoised volume. Figure 12c, d depict the overlay of the morphological reconstruction (red) with the denoised volume (white). Given a manual reconstruction M_1 and the automatic reconstructed tree P_1 , the reconstruction error for a point in $p \in P_1$ is defined as the minimum distance from p to the points in the manual reconstruction M_1 . The mean error (\mathcal{E}) is defined as the mean of the reconstruction error for all the points in P_1 . The mean error \mathcal{E} from the reconstructed morphological model was found to be equal to 1.62 voxels with a standard deviation of 0.69 voxels, while the number of branching points was 75 compared to 57 branching points obtained from ORION. Processing time was 284 s.

Pyramidal Neurons Pyramidal neurons were acquired as a sequence of sub-volumes V_1, \dots, V_n , where $V_i: \mathbb{R}^3 \rightarrow \mathbb{R}$ and $i \leq n$. We applied the method reported in Santamaría-Pang et al. (2008) to denoise each sub-volume. Then a denoised volume is created by merging the denoised sub-volumes. The translation parameter $T_{i,i+1}$, along the x , y , and z axes was provided by the experimentalist, and corresponded to the fields of view when moving the microscope's stage.

Figures 13 and 14 depict the results of our method and Sato et al. (1998). Figure 13a, c, e depict the maximum intensity projection of the denoised volume, the result of Sato's method, and ORION, respectively. Figure 13b, d, f depict the detail of the original volume, the results obtained using Sato's method, and ORION, respectively. Note the difference for the enhancement of the dendrite, particularly regions with spines.

The dataset used for performance evaluation corresponds to three cells of interest depicted in the selected volumes were ranked according to image quality- good, medium, and poor. Cells A and B were acquired by using a multiphoton microscope. Figure 15a, b depict images of good and medium quality, respectively. The volume corresponding to the cell C was acquired using a confocal microscope and the image quality was ranked to be poor, as depicted in Fig. 15c.

To assess the quality of ORION (OR), we compared both qualitatively and quantitatively our results with those obtained from two human experts: E1 and

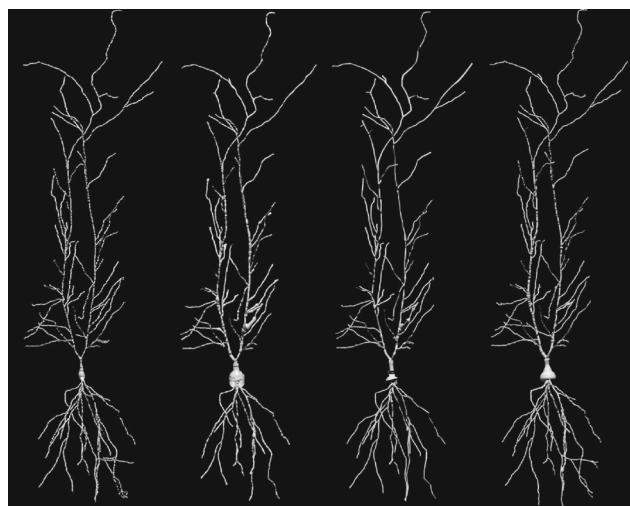


Fig. 16 A qualitative comparison of morphological reconstructions. From left to right, the morphological reconstruction obtained using OR, the computer tracer (AN) and the human tracers E1 and E2, respectively

E2, and from one tracer using the module Auto Neuron (AN) from NeuroLucida™. The comparative analysis revealed the efficiency of the different methods in representing the branch lengths, diameters, and connectivity. Visual comparison demonstrated the success of each method in capturing the morphology. A qualitative comparison of the morphological reconstructions is depicted in Fig. 16 (from left to right: OR, AN, and human experts E1, E2).

A comparison of the tree representation among all the tracers for cell A is depicted in Fig. 17. Figure 17a is a depiction of the reconstructed tree using ORION, Fig. 17b is a depiction of the reconstruction using AN, and Fig. 17c, d depict the reconstruction obtained from the human experts. The height of the tree for ORION, AN, E1, and E2 is 19, 25, 21, and 21, respectively. The tree with the maximum

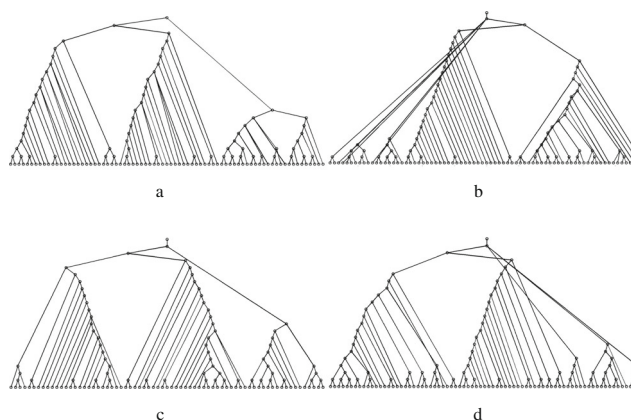


Fig. 17 (a–d) The tree representation of the morphological reconstruction for OR, AN, and experts E1 and E2, respectively

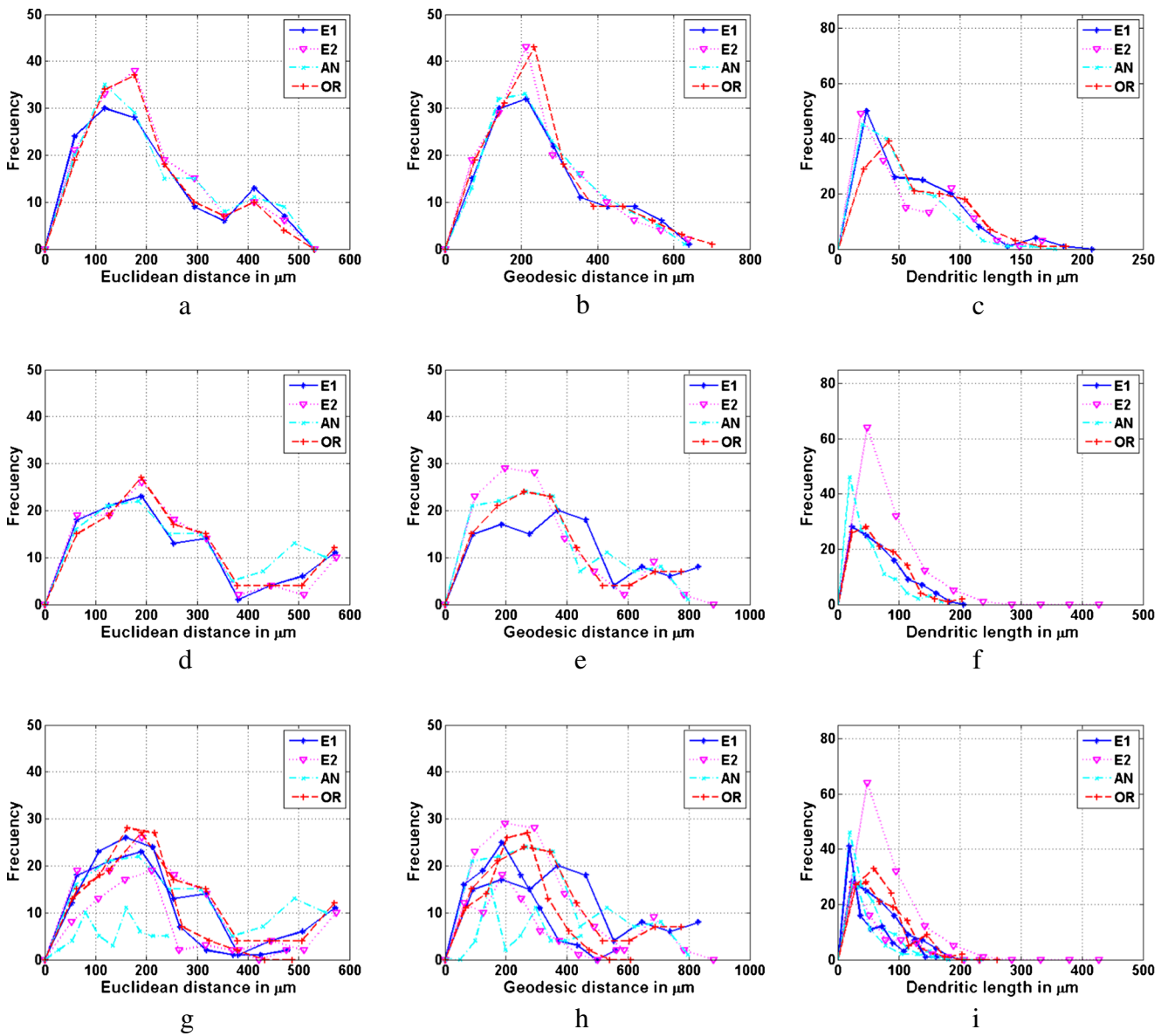


Fig. 18 Sholl analysis for cells A, B, and C: **(a, d, g)** a comparison of the number of branches as a function of Euclidean Distance (*ED*) from the soma; **(b, e, h)** number of branches as a function of the

Geodesic Distance (*GD*) of the branching point to the soma; **(c, f, i)** a depiction of the distribution of Dendritic Length (*DL*)

height was from AN, while the tree with lowest height corresponded to ORION.

To quantitatively compare, both globally and locally, the reconstructed cell topology among all reconstructions, a

Table 1 Performance Evaluation - Total Dendritic Length (μm) and Number of Branching Points (*P*)

	Cell A		Cell B		Cell C	
	Length (μm)	<i>P</i>	Length (μm)	<i>P</i>	Length (μm)	<i>P</i>
E1	6,327	66	6,353	54	4,017	46
E2	6,805	73	6,588	54	3,397	33
AN	5,698	66	5,059	60	1,607	23
OR	7,417	66	6,913	55	5,593	45

Table 2 Empirical Distribution Parameters of Lengths of Segments between Nodes (μm)

	Cell A				Cell B				Cell C			
	μ	σ	min	max	μ	σ	min	max	μ	σ	min	max
E1	46.52	39.90	0.23	208.38	56.72	43.34	0.28	206.04	40.50	39.30	0.20	161.20
E2	45.37	38.89	1.07	167.61	57.28	56.60	0.00	427.64	51.00	46.10	1.10	232.10
AN	40.48	33.27	0.30	177.97	40.47	36.65	0.82	168.79	42.20	43.20	2.00	232.10
OR	53.07	37.81	4.72	186.88	57.57	40.92	5.04	203.39	55.93	41.61	4.99	261.31

variant of Sholl analysis (Rall 1977; Sholl 1953; Pelt and Schierwagen 2004; Mizrahi et al. 2000) was used. Global descriptors include: (i) the total dendritic length and (ii) the length statistics per segment.

Local descriptors (Sholl 1953; Uylings and van Pelt 2002) include the number of branching points as a function of: (i) the Euclidean Distance (ED); (ii) the Geodesic Distance (GD) to the soma measured on the centerline; and (iii) the distribution of Dendritic Lengths (DL) measured on the centerline. Figure 18 presents a quantitative comparison with respect to the metrics ED and GD among all the tracers in cells A, B, and C.

Figure 18(c, f, i) depict a quantitative comparison in cells A, B, and C with respect to the metrics DL. Note that the largest discrepancy occurs for the “good” neuron in which the smallest variance would be expected (as a result of the dye-filling that produces a bright consistent signal). Using quantitative global descriptors, all of the tracers reported longer dendritic lengths when given higher quality datasets due to the larger signals in the distal and thin processes.

Table 1 presents the total dendritic length and number of branching points. Note that ORION results as the method that detect more total dendrite length for each of the cells. This is mainly because ORION is able to detect paths in low intensity dendrites which are difficult to trace by humans.

The AN tracer consistently reported the smallest dendritic length, which may be explained by the fact that it does not automatically reconnect discontinuous branches. ORION reported the longest total dendritic lengths for all three datasets. This can be explained due the fact that ORION is able to detect paths in dendrites with low intensity which are difficult to trace by humans. Note that the

number of detected branching points from ORION and the manual tracer E1 are very similar. In addition, E1 and E2 reported 54 branching points for cell B while ORION reported 55. Tables 2 and 3 report the statistics of the total dendritic lengths. The inherent variability between manual tracings is highlighted by the fact that each tracing was performed over several hours, possibly spanning multiple days, and each dataset was addressed over the span of several weeks. For the “good” and average datasets, the two tracers reported an average dendritic length that was within a $1.15 \mu m$ and $0.56 \mu m$ range (close agreement), respectively. The average dendritic lengths for the “poor” datasets were spread over a larger range ($10.5 \mu m$). No tracer was consistent at either extreme.

Local descriptors indicate the “completeness” of the morphological reconstruction. With respect to ED (Fig. 18(a, d, g)), all of the tracers had a similar performance in cell A (good quality), a comparable performance in cell B (medium quality), and significant differences in cell C (poor quality).

Consistent results were obtained with respect to the GD measure, as depicted in Fig. 18(b, e, h). These results suggest that all tracers agree that GD reaches the largest frequency at $200 \mu m$ in cell A. E2, AN and ORION agree that the highest frequency in cell B is close to $250 \mu m$. Finally, there is not agreement between the tracers in cell C. Similar results were obtained when computing the dendritic lengths (Fig. 18(c, f, i)). A relative amount of consistency was obtained among the tracers in cell A, whereas a relative amount of discrepancy was obtained in cell C.

Figures 19 and 20 depict the rest of our cell database consisting of those cells acquired from the multiphoton

Table 3 Empirical Distribution Parameters of Path Lengths from Soma (μm)

	Cell A				Cell B				Cell C			
	μ	σ	min	max	μ	σ	min	max	μ	σ	min	max
E1	266.63	135.25	93.38	640.29	390.93	222.62	54.96	830.44	216.27	113.40	61.61	559.44
E2	253.05	130.88	81.97	637.95	312.05	197.32	42.60	882.00	225.96	114.82	50.48	563.26
AN	250.18	135.18	61.70	628.83	316.40	184.30	55.55	796.42	247.18	107.37	101.99	444.75
OR	256.64	139.00	79.02	700.51	338.19	194.34	69.41	776.19	234.63	111.76	37.57	608.44

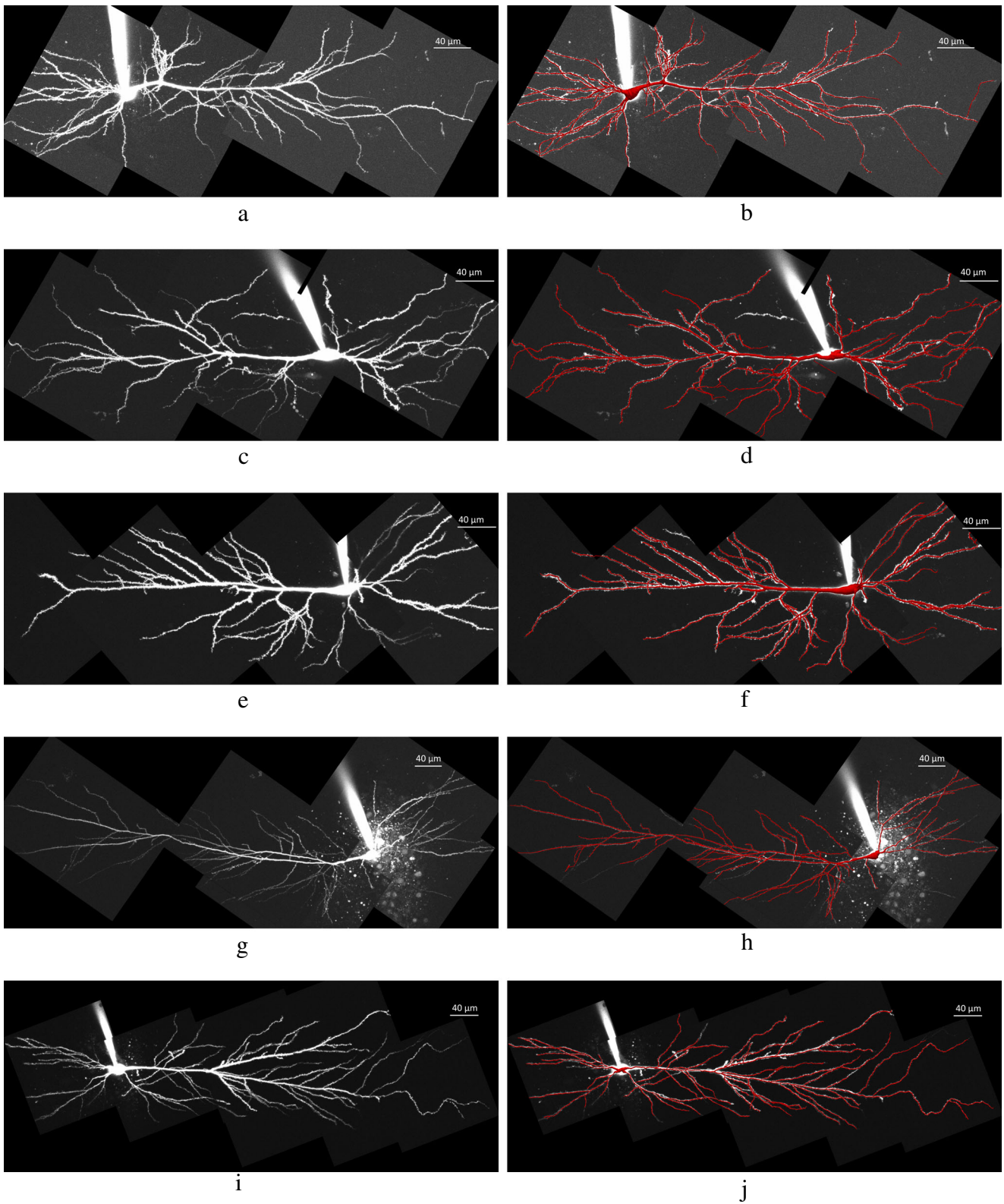


Fig. 19 Depiction of the morphological reconstruction for different cells: **a, c, e, g, i** maximum intensity projections of cells D through H, respectively, **b, d, f, h, j** morphological reconstruction for cells D through H, respectively

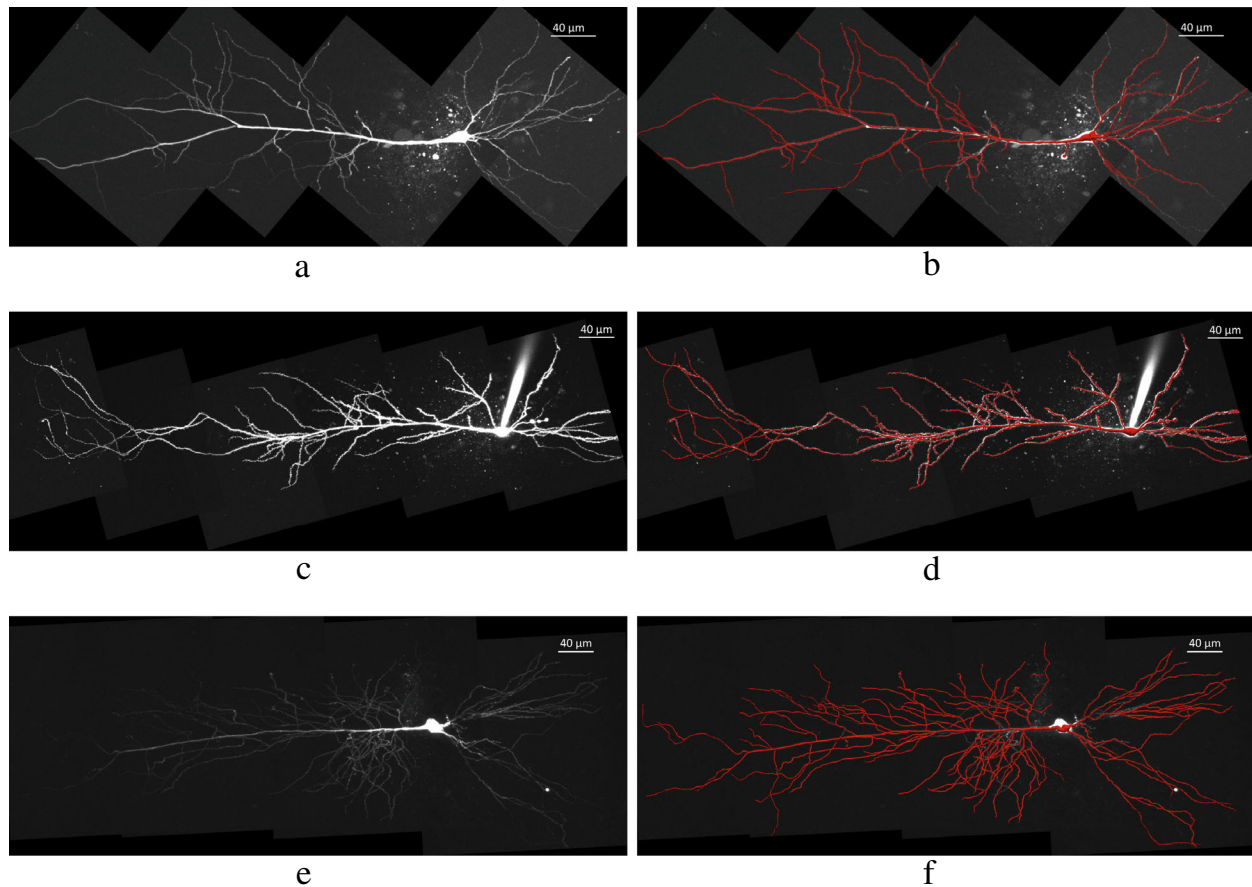


Fig. 20 Depiction of the morphological reconstruction for different cells: **a, c, e** maximum intensity projections of cells I through K, respectively, **b, d, f** morphological reconstruction for cells I through K, respectively

and confocal microscopes (from cell D to cell K). The left column depicts the maximum intensity projection of the denoised volumes, while the right column depicts the

result of ORION. Note that some cases are very challenging, specifically for the cells G, I, J, and K (Figs. 19g and 20(a, c, e)) which contain high levels of structural noise, specifically near the soma.

Table 4 Summary of Reconstruction Time (RT), Total Dendritic Length (μm) and Number of Branching Points (P)

Cell Database				
	Size	RT (hours)	Length (μm)	P
Cell A	$2,546 \times 912 \times 121$	0.71	7,417	66
Cell B	$1,123 \times 2,357 \times 146$	0.84	6,913	55
Cell C	$1,127 \times 3,172 \times 199$	2.11	5,593	45
Cell D	$1,568 \times 1,160 \times 145$	0.52	6,910	66
Cell E	$1,400 \times 1,057 \times 152$	0.54	5,638	48
Cell F	$1,538 \times 1,525 \times 125$	0.48	5,350	48
Cell G	$1,742 \times 1,302 \times 115$	1.21	5,356	56
Cell H	$1,668 \times 959 \times 45$	0.22	7,111	48
Cell I	$1,612 \times 1,329 \times 84$	0.34	5,239	50
Cell J	$1,204 \times 2,995 \times 174$	2.38	10,233	93

Table 5 Empirical Distribution Parameters of Centerline Detection Error \mathcal{E}

Dataset	Volume	μ (voxels)	σ (voxels)
1	Cerebellar CF_1	4.34	2.73
	Cerebellar CF_2	3.87	2.49
3	Neocortical	2.04	1.12
4	Neuromuscular	5.94	4.72
5	Olfactory OP1	1.05	0.61
	Olfactory OP3	1.10	0.58
	Olfactory OP4	1.17	0.69
	Olfactory OP5	1.04	0.59
	Olfactory OP6	1.12	0.63
	Olfactory OP7	1.12	0.59
	Olfactory OP8	0.94	0.51
	Olfactory OP9	1.15	0.64

Table 6 Performance Evaluation on the OP Dataset

Method	Precision	Recall	MES
Neurostudio	0.97	0.81	0.79
APP2	0.73	0.88	0.71
ORION	0.95	0.86	0.92

Table 4 presents a performance analysis of our method for the cell database consisting of eleven cells. Cell J (Fig. 20d) corresponds to the cell with the largest dendrite length (10,233 μm) while cell I (Fig. 20b) had the shortest dendrite length (5,239 μm). The cell with the largest number of dendritic points was cell J (Fig. 20d) and the shortest was cell C (Fig. 19f). Also note that cell H corresponded to the shortest time in reconstruction and the cell with the longest reconstruction time was cell J (Fig. 19c). The dimensions of each individual volume are reported in the second column.

Finally, we present the results obtained on the DIADEM data. Our ORION method was applied to four out of six datasets with varying levels of success. The performance results of ORION on these datasets is presented in Table 5.

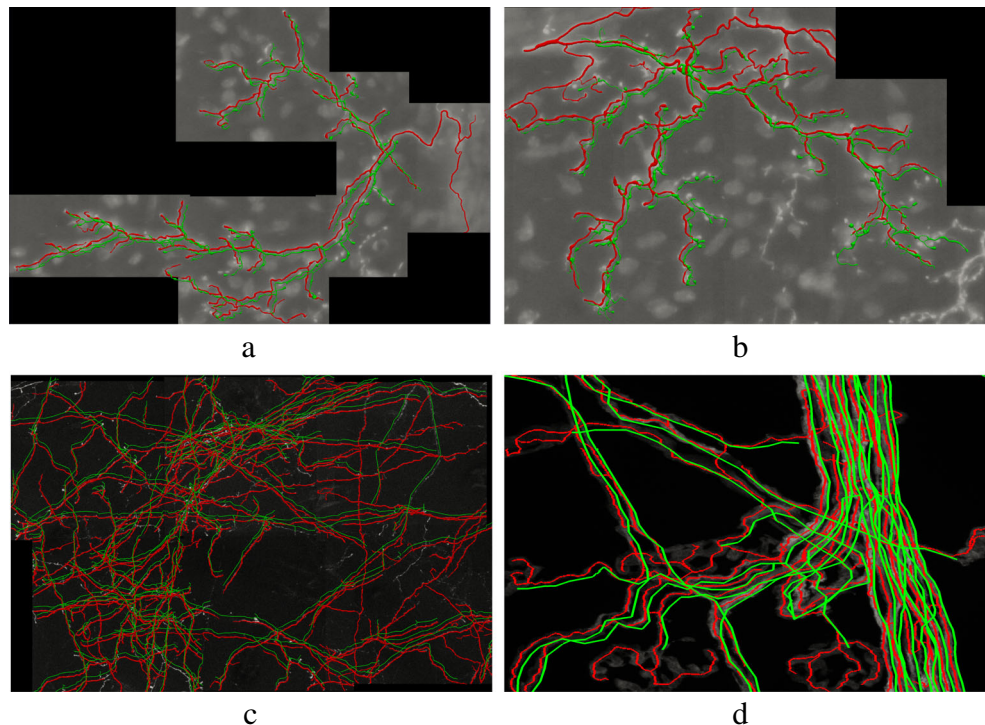
DIADEM dataset For each of the DIADEM datasets, we train an SVM classifier. We optimize the parameters C (cost) and g (gamma) of the SVM classifier by applying a grid search and 2-fold cross validation. We manually selected positive samples to train the SVM classifier from

a wide range of variation in the morphology of the training volume (e.g., thin and thick dendrites, dendrites with low and high curvature, and positions where the dendrites bifurcate or tri-furcate). In addition, negative samples correspond to background with the requirement that they are close to positive samples.

In our experiments, we disabled the soma center-point detection since the datasets do not capture a cell's soma. The soma vertex s_0 for each volumes in the DIADEM dataset was selected as the provided root coordinates for the reconstruction.

We present qualitative and quantitative results in four datasets from the DIADEM challenge (Brown et al. 2011). One of the reviewers strongly suggested correcting the DIADEM manual reconstructions first by adding the missing branches and fixing the misconnections, and then computing the DIADEM metric scores (Gillette et al. 2011) for the reconstructions. We did modify the manual reconstruction to include missed branches for the Olfactory Projection Fibers dataset in order to correctly compute the values of Precision, Recall and MES. However, we did not use the DIADEM metric to quantitatively compare the reconstruction against the ground truth for three reasons (these issues have also been pointed out in (Chothani et al. 2011; Mayerich et al. 2012; Ming et al. 2013; Basu et al. 2014)). First, the DIADEM metric employs higher penalties for errors closer to the root. This strategy is acceptable if the root position is selected to be the soma. However, the soma is not the root position for all the DIADEM datasets. Second, the

Fig. 21 Depiction of the morphological reconstruction for the DIADEM dataset: **a**, **b** dataset 1 volume CF1, CF2, **c** neocortical dataset, **d** neuromuscular dataset stack 115. Green line represents the ground truth, and red line depicts the reconstruction with OR



DIADEM metric offers lower scores to trees with gaps since the metric only accounts for connected trees. Third, there may be some errors in the gold standard, which may result on not attaining perfect score even if the reconstruction is correct.

Figure 23 presents comparison of the cell reconstruction using our method (red color) and the manual reconstruction (green color) in DIADEM datasets. Note that to visualize both reconstructions, the DIADEM reconstruction was

translated in the xy direction. Figure 21a, b depict the reconstructions from cerebellar climbing fiber image stacks acquired with transmitted light brightfield microscopy; in general there is agreement in the reconstruction. Table 5 presents the estimated error with respect to the manual annotations provided by the DIADEM challenge. We note that the largest error was in dataset 4. The reason for this disagreement is due to the large size of the cells to detect. The smallest was in the olfactory OP1 cell. The metrics

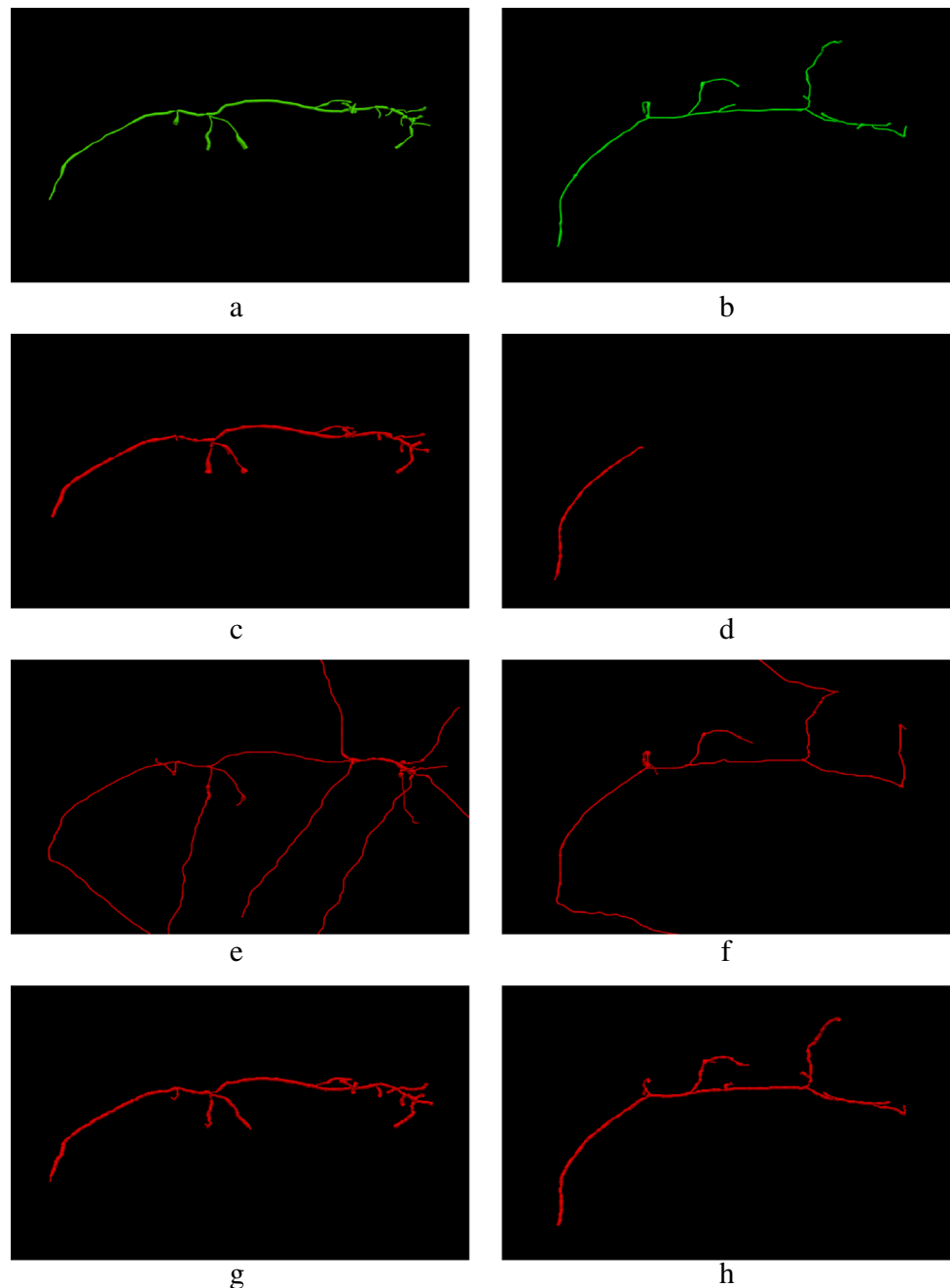


Fig. 22 **a, b** Manual reconstruction from two volumes of the OP dataset. **c, d** Reconstruction from the Neurostudio software by selecting a single seed point, **e, f** result from the APP2 method and **g, h** ORION centerline extraction

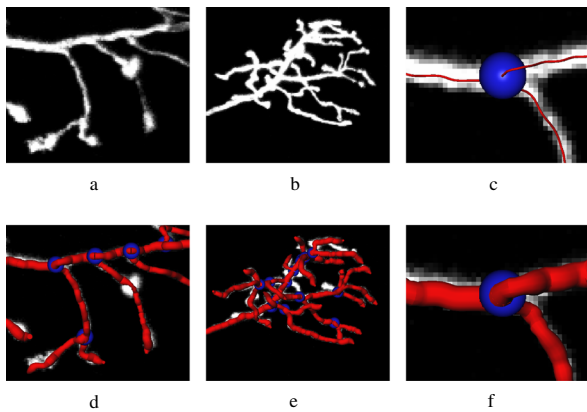


Fig. 23 A depiction of centerline extraction and diameter estimation: **a, b, c** a depiction of a maximum intensity projection of the denoised volume; **d, e, f** overlay of the maximum intensity projection of the denoised data with the detected centerline (red) and the detected bifurcation point (sphere with blue color)

Precision, Recall and Miss-Extra-Score (MES) are used to qualitatively measure the performance of ORION. Precision = S_C/S_T , Recall = $S_C/(S_C + S_m)$ and Miss-Extra-Score (MES) = $(S_G - S_m)/(S_G + S_e)$, where S_C is the total length of the correct segments by each algorithm and S_T and S_G are the total lengths of the traced centerline by the algorithm tested and by an expert, respectively. The symbols S_m and S_e are the total length of missing and extra segments in the automatically traced, respectively. ORION was compared against publicly available automatic neuron reconstruction algorithms (Neurostudio (Wearne et al. 2005) and APP2 (Xiao and Peng 2013)). Table 6 summarizes the average result of the metrics in eight out of nine volumes from the Olfactory Projection Fibers dataset. Note that a volume was not used for comparison since it contains two neurons and only the manual reconstruction for one of them was

provided. Our method provides the best results for MES, indicating that it results in more accurate reconstruction of the neurons. In addition, the results of the metric Precision and Recall from our method are very close to the best results with only a difference of 0.02. Figure 22a, b depict the manual reconstruction of two of the 3D image stacks from the OP dataset. Figure 22c–h depict the reconstruction by Neurostudio, APP2 and ORION, respectively. Note that Neurostudio misses some branches while APP2 produces spurious branches.

Figure 23 depicts the different anatomical branches for which the morphological model is extracted from cell OP.1. Figure 23c depicts a bifurcation branch overlapped with the extracted centerline (line in red) and the sphere in blue is the detected branching point. Figure 23d–e depict the estimated cylindrical representation of three anatomical structures.

Our ORION software has been used (for example) at the Brenowitz Laboratory at the University of Washington (UWBL), which focuses on select aspects of neurogenesis. Specifically, they investigate seasonal neuronal turnover in the song circuitry of the male white crowned sparrow. While neurogenesis occurs in the subventricular zone at a fairly constant rate, new neurons are recruited and integrated in the HVC at the onset of the breeding season. Under androgenic and circadian control, these neurons establish the circuitry required for song development. Upon cessation of the androgenic stimulus, select neurons undergo apoptosis to restore a non-breeding state. UWBL is particularly interested in the cell signalling components and the developing neuronal network. With the help of the ORION software they reconstruct existing neurons pre- and post stimulation (Fig. 24). The software greatly accelerates their ability to morphologically characterize these neurons and to better understand their role in the establishment of neuronal networks.

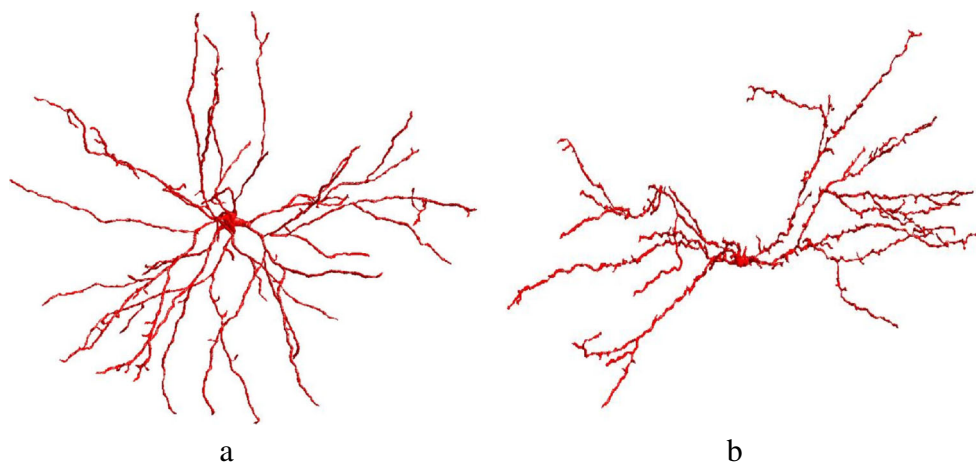


Fig. 24 Sample neurons found in the HVC. **a** Pre-stimulation. **b** Post-stimulation

Conclusions

In this paper, we presented a general framework for creating an automatic 3D morphological reconstruction of pyramidal neuronal cells from optical images. Specifically, we presented: (i) a new method for enhancing regular and irregular tubular, tree-type structures without assuming a particular tubular shape; (ii) an automatic algorithm for 3D reconstruction of such structures with sub-voxel accuracy, primarily applied on pyramidal neuronal cells and (iii) and a post-processing step to correct topological errors from the morphological reconstruction such as the detection of crossings and the connection of near optimal paths.

The proposed dendrite detection method generalizes the classical approaches for the detection of tubular structures and demonstrates that it is possible to robustly detect neuron dendrites in optical images. In addition, the proposed method enhances dendritic spines and demonstrates itself to be robust to variations in shape and scale. The experimental results demonstrate that the proposed method is highly accurate in recovering the geometry of the pyramidal neuronal cells.

Information Sharing Statement

ORION software (RRID:nlx_56302) and documentation can be requested at <http://cbl.uh.edu/ORION/research/software> (no fee license). Our software is written in Matlab R2013 and ITK. It is developed for Windows users, hence some routines have to be compiled for other OS. The DIADEM dataset (RRID:nif-0000-23194) can be downloaded from http://www.diaDEMchallenge.org/data_sets.html.

Acknowledgments We wish to thank all of the members of the ORION team (Computational Biomedicine Lab 2014) and especially Costa M. Colbert, Yong Liang, and Bradley E. Losavio. The data were acquired at P. Saggau's Laboratory in the Department of Neuroscience of the Baylor College of Medicine. This work was supported in part by NIH 5R01EB001048-02, NSF-DMS 0915242, NHARP 003652-0136-2009 and the University of Houston–Eckhard Pfeiffer Endowment Fund. Any opinions, findings, conclusions or recommendations expressed in this material are those of the authors and may not reflect the views of UH, NIH, NHARP, or NSF.

References

- Bas, E., & Erdogmus, D. (2011). Principal curves as skeletons of tubular objects. *Neuroinformatics*, 9(2–3), 181–191.
- Basu, S., Ooi, W.T., Racoceanu, D. (2014). Improved marked point process priors for single neurite tracing. In *IEEE international workshop on Pattern recognition in neuroimaging* (pp. 1–4).
- Breitenreicher, D., Sofka, M., Britzen, S., Zhou, S. (2013). Hierarchical discriminative framework for detecting tubular structures in 3D images. In J. Gee (Ed.) *Proceedings of information processing in medical imaging, Lecture Notes in computer Science* (Vol. 7917, pp. 328–339). Asilomar, CA: Springer-Verlag Berlin Heidelberg.
- Broser, P., Schulte, R., Roth, A., Helmchen, F., Lang, S., Wittum, G., Sakmann, B. (2004). Nonlinear anisotropic diffusion filtering of three-dimensional image data from two-photon microscopy. *Journal of Biomedical Optics*, 9(6), 1253–1264.
- Brown, K., Barrionuevo, G., Canty, A., Paola, V., Hirsch, J., Jefferis, G., Lu, J., Snippe, M., Sugihara, I., Ascoli, G. (2011). The DIADEM data sets: representative light microscopy images of neuronal morphology to advance automation of digital reconstructions. *Neuroinformatics*, 9(2-3), 143–157.
- Chothani, P., Mehta, V., Stepanyants, A. (2011). Automated tracing of neurites from light microscopy stacks of images. *Neuroinformatics*, 9(2–3), 263–278.
- Computational Biomedicine Lab (2014). ORION: Online Reconstruction and functional Imaging Of Neurons. <http://www.cbl.uh.edu/ORION>.
- Cortes, C., & Vapnik, V. (1995). Support-vector networks. *Machine Learning*, 20(3), 273–297.
- Cuntz, H., Forstner, F., Borst, A., Häusser, M., Morrison, A. (2010). One rule to grow them all: A general theory of neuronal branching and its practical application. *PLoS Computational Biology*, 6(8).
- Diestel, R. (2005). *Graph theory*. Berlin Heidelberg New York: Springer.
- Dijkstra, E. (1959). A note on two problems in connection with graphs. *Numerische Mathematica*, 1, 269–271.
- Dima, A., Scholz, M., Obermayer, K. (2002). Automatic segmentation and skeletonization of neurons from confocal microscopy images based on the 3-D wavelet transform. *IEEE Transactions on Image Processing*, 11(7), 790–801.
- Duke/Southampton (2013). Neuroscience research group, school of biological sciences, southampton university: Duke/southampton archive of neuronal morphology. <http://neuron.duke.edu/cells/>.
- Evers, J., Schmitt, S., Sibila, M., Duch, C. (2005). Progress in functional neuroanatomy: Precise automatic geometric reconstruction of neuronal morphology from confocal image stacks. *Journal of Neurophysiology*, 93(4), 2331–2342.
- Frangi, A., Niessen, W., Vincken, K., Viergever, M. (1998). Multiscale vessel enhancement filtering. In *Proceedings of medical image computing and computer assisted intervention*, (Vol. 1496 pp. 130–137). Cambridge, MA.
- Gillette, T., Brown, K., Ascoli, A. (2011). The DIADEM metric: comparing multiple reconstructions of the same neuron. *Neuroinformatics*, 9(2–3), 233–245.
- Gonzalez, G., Fleuret, F., Fua, P. (2009). Learning rotational features for filament detection. In *Proceedings of IEEE computer society conference on computer vision and pattern recognition* (pp. 1582–1589). Miami Beach, FL.
- González, G., Turetken, E., Fleuret, F., Fua, P. (2010). Delineating trees in noisy 2D images and 3D image-stacks. In *Proceedings of IEEE computer society conference on computer vision and pattern recognition* (pp. 2799–2806). San Francisco, CA.
- Greenspan, H., Laifenfeld, M., Einav, S., Barnea, O. (2001). Evaluation of center-line extraction algorithms in quantitative coronary angiography. *IEEE Transactions on Medical Imaging*, 20(9), 928–941.
- Hassouna, M., Farag, A., Falk, R. (2005). Differential Fly-Throughs (DFT): A general framework for computing flight paths. In *Proceedings of medical image computing and computer-assisted intervention*, (Vol. 1 pp. 654–661). PalmSprings, CA.
- Kakadiaris, I., Santamaría-Pang, A., Colbert, C., Saggau, P. (2008). Automatic 3-D morphological reconstruction of neuron cells from

- multiphoton images. In J. Rittscher, R. Machiraju, S. Wong (Eds.) *Microscopic image analysis for life science applications*, (pp. 389–399). Norwood, MA: Artech House.
- Lorenz, C., Carlsen, I., Buzug, T., Fassnacht, C., Weese, J. (1997). Multi-scale line segmentation with automatic estimation of width, contrast and tangential direction in 2D and 3D medical images. In *Proceedings of first joint conference on computer vision, virtual reality and robotics in medicine and medial robotics and computer-assisted surgery*, (Vol. 1205 pp. 233–244).
- Losavio, B., Liang, Y., Santamaría-Pang, A., Kakadiaris, I., Colbert, C., Saggau, P. (2008). Live neuron morphology automatically reconstructed from multiphoton and confocal imaging data. *Journal of Neurophysiology*, 100, 2422–2429.
- Mayerich, D., Bjornsson, C., Taylor, J., Roysam, B. (2012). NetMets: software for quantifying and visualizing errors in biological network segmentation. *BMC bioinformatics*, 13(Suppl 8), S7.
- Meijering, E. (2010). Neuron tracing in perspective. *Cytometry Part A*, 77A(7), 693–704.
- Ming, X., Li, A., Wu, J., Yan, C., Ding, W., Gong, H., Zeng, S., Liu, Q. (2013). Rapid reconstruction of 3D neuronal morphology from light microscopy images with augmented rayburst sampling. *PLoS one*, 8(12), e84557.
- Mizrahi, A., Ben-Ner, E., Katz, M., Kedem, K., Glusman, J., Libersat, F. (2000). Comparative analysis of dendritic architecture of identified neurons using the Hausdorff distance metric. *The Journal of Comparative Neurology*, 233(3), 415–428.
- NeuroLucida (2014). MBF Bioscience: stereology and neuron morphology quantitative analysis. <http://www.mbfioscience.com>.
- Pawley, J. (2006). *Handbook of Biological Confocal Microscopy*. New York: Springer-Verlag.
- Pelt, J.v., & Schierwagen, A. (2004). Morphological analysis and modeling of neuronal dendrites. *Mathematical Biosciences*, 188(1-2), 147–155.
- Peng, H., Long, F., Myers, G. (2011). Automatic 3D neuron tracing using all-path pruning. *Bioinformatics*, 27(13), i239.
- Perona, P., & Malik, J. (1990). Scale-space and edge detection using anisotropic diffusion. *IEEE Transactions on Pattern Analysis and Machine Intelligence*, 12(7), 629–639.
- Platt, J.C. (2000). Probabilistic outputs for support vector machines and comparison to regularize likelihood methods. *Advances in large margin classifiers*, (pp. 61–74).
- Rall, W. (1977). *Handbook of Physiology: The Nervous System. Chapter Core conductor theory and cable properties of neurons* (Vol. 1, pp. 39–98). Baltimore, MD: American Physiological Society Bethesda.
- Rosenfeld, A., & Pfaltz, J. (1968). Distance functions on digital pictures. *Pattern Recognition*, 1(1), 33–61.
- Rouchdy, Y., & Cohen, L. (2009). The shading zone problem in geodesic voting and its solutions for the segmentation of tree structures. application to the segmentation of microglia extensions. In *Proceedings of computer vision and pattern recognition workshops* (pp. 66–71). Miami.
- Santamaría-Pang, A., Bildea, T., Colbert, C., Saggau, P., Kakadiaris, I. (2006). Towards segmentation of irregular tubular structures in 3D confocal microscope images. In *Proceedings of miccai workshop in microscopic image analysis and applications in biology* (pp. 78–85). Denmark, Copenhagen.
- Santamaría-Pang, A., Colbert, C., Losavio, B., Saggau, P., Kakadiaris, I. (2007a). Automatic morphological reconstruction of neurons from optical images. In *Proceedings of international workshop in microscopic image analysis and applications in biology*. Piscataway.
- Santamaría-Pang, A., Colbert, C., Saggau, P., Kakadiaris, I. (2007b). Automatic centerline extraction of irregular tubular structures using probability volumes from multiphoton imaging. In *Proceedings of medical image computing and computer-assisted intervention* (pp. 486–494). Brisbane.
- Santamaría-Pang, A., Bildea, T., Tan, S., Kakadiaris, I. (2008). Denoising for 3-D photon-limited imaging data using nonseparable filterbanks. *IEEE Transactions on Image Processing*, 17(12), 2312–2323.
- Sato, Y., Nakajima, S., Atsumi, H., Koller, T., Gerig, G., Yoshida, S., Kikinis, R. (1998). 3-D multi-scale line filter for segmentation and visualization of curvilinear structures in medical images. *Medical Image Analysis*, 2(2), 143–168.
- Sethian, J. (1996). *Level Set Methods: Evolving Interfaces in Geometry, Fluid Mechanics, Computer Vision and Materials Sciences*. Cambridge: Cambridge University Press.
- Sholl, D. (1953). Dendritic organization in the neurons of the visual and motor cortices of the cat. *Journal of Anatomy*, 87(4), 387–406.
- Srinivasan, R., Li, Q., Zhou, X., Lu, J., Lichtman, J., Wong, S. (2010). Reconstruction of the neuromuscular junction connectome. *Bioinformatics*, 26(12), i64–i70.
- Turetken, E., Benmansour, F., Fua, P. (2012). Automated reconstruction of tree structures using path classifiers and mixed integer programming. In *Proceedings of IEEE conference on computer vision and pattern recognition (CVPR)* (pp. 566–573). Rhode Island.
- Turetken, E., Benmansour, F., Andres, B., Pfister, H., Fua, P. (2013). Reconstructing loopy curvilinear structures using integer programming. In *Proceedings of the IEEE, CVPR* (pp. 1822–1829). Portland.
- Uehara, C., Colbert, C.M., Saggau, P., Kakadiaris, I. (2004). Towards automatic reconstruction of dendrite morphology from live neurons. In *Proceedings of 26th annual international conference of the IEEE engineering in medicine and biology society* (pp. 1798–1801). San Francisco.
- Urban, S., O'Malley, S.M., Walsh, B., Santamaría-Pang, A., Saggau, P., Colbert, C., Kakadiaris, I. (2006). Automatic reconstruction of dendrite morphology from optical section stacks. In *Proceedings of 2nd international workshop on computer vision approaches to medical image analysis* (pp. 190–201). Graz: Springer.
- Uyulings, H., & van Pelt, J. (2002). Measures for quantifying dendritic arborizations. *Network: Computation in Neural Systems*, 13(3), 397–414.
- Vapnik, V. (1995). *The Nature of Statistical Learning Theory*. Berlin: Springer-Verlag.
- Vasilkoski, Z., & Stepanyants, A. (2009). Detection of the optimal neuron traces in confocal microscopy images. *Journal of Neuroscience Methods*, 178(1), 197–204.
- Wang, Y., Narayanaswamy, A., Roysam, B. (2011a). Novel 4-D open-curve active contour and curve completion approach for automated tree structure extraction. In *Proceedings of the IEEE conference on computer vision and pattern recognition. IEEE* (pp. 1105–1112). Colorado Springs.
- Wang, Y., Narayanaswamy, A., Tsai, C.-L., Roysam, B. (2011b). A broadly applicable 3-D neuron tracing method based on open-curve snake. *Neuroinformatics*, 9(2-3), 193–217.
- Wearne, S., Rodriguez, A., Ehlenberger, D., Rocher, A., Henderson, S., Hof, P. (2005). New techniques for imaging, digitization and analysis of three-dimensional neural morphology on multiple scales. *Neuroscience*, 136(3), 661–680.
- Xiao, H., & Peng, H. (2013). APP2: automatic tracing of 3D neuron morphology based on hierarchical pruning of a gray-weighted image distance-tree. *Bioinformatics*, 29(11), 1448–1454.
- Xie, J., Zhao, T., Lee, T., Myers, E., Peng, H. (2010). Automatic neuron tracing in volumetric microscopy images with anisotropic path Searching. In *Proceedings of the medical image*

- computing and computer-assisted intervention* (pp. 472–479). Beijing.
- Xie, J., Zhao, T., Lee, T., Myers, E., Peng, H. (2011). Anisotropic path searching for automatic neuron reconstruction. *Medical image analysis*, 15(5), 680–689.
- Yuan, X., Trachtenberg, J., Potter, S., Roysam, B. (2009). MDL constrained 3-D grayscale skeletonization algorithm for automated extraction of dendrites and spines from fluorescence confocal images. *Neuroinformatics*, 7, 213–232.
- Zhao, T., Xie, J., Amat, F., Clack, F., Ahammad, P., Peng, H., Long, F., Myers, E. (2011). Automated reconstruction of neuronal morphology based on local geometrical and global structural models. *Neuroinformatics*, 9(2-3), 247–261.
- Zhao, Y., Xiong, H., Zhang, K., Zhou, X. (2009). Equilibrium modeling for 3D curvilinear structure tracking of confocal microscopy images. In *Proceedings of the IEEE international conference on image processing* (pp. 2533–2536). Cairo.